Deconvolution of reacting-flow dynamics using proper orthogonal and dynamic mode decompositions

Sukesh Roy, Jia-Chen Hua, Will Barnhill, Gemunu H. Gunaratne, and James R. Gord

Deconvolution of Reacting-Flow Dynamics Using Proper Orthogonal and Dynamic Mode Decompositions

Sukesh Roy*

Spectral Energies, LLC, Dayton, OH 45431

Jia-Chen Hua, Will Barnhill, and Gemunu H. Gunaratne

Department of Physics, University of Houston, Houston, TX 77204

James R. Gord

Aerospace Systems Directorate, Air Force Research Laboratory, WPAFB, OH 45433

(Dated: December 11, 2014)

Abstract

Analytical and computational studies of reacting flows are extremely challenging due in part to nonlinearities of the underlying system of equations and long-range coupling mediated by heat and pressure fluctuations. However, many dynamical features of the flow can be inferred through low-order models if the flow constituents (*e.g.,* eddies or vortices) and their symmetries, as well as the interactions among constituents, are established. Modal decompositions of high-frequency, high-resolution imaging, such as measurements of species-concentration fields through planar laser-induced florescence (PLIF) and of velocity fields through particle-image velocimetry (PIV), are the first step in the process. A methodology is introduced for deducing the flow constituents and their dynamics following modal decomposition.

Proper orthogonal (POD) and dynamic mode (DMD) decompositions of two classes of problems are performed and their strengths compared. The first problem involves a cellular state generated in a flat circular flame front through symmetry breaking. The state contains two rings of cells that rotate clockwise at different rates. Both POD and DMD can be used to deconvolve the state into the two rings. In POD the contribution of each mode to the flow is quantified using the energy. Each DMD mode can be associated with an energy as well as a unique complex growth rate. Dynamic modes with the same spatial symmetry but different growth rates are found to be combined into a single POD mode. Thus, a flow can be approximated by a smaller number of POD modes. On the other hand, DMD provides a more detailed resolution of the dynamics.

Two classes of reacting flows behind symmetric bluff bodies are also analyzed. In the first, symmetric pairs of vortices are released periodically from the two ends of the bluff body. The second flow contains von Karman vortices also, with a vortex being shed from one end of the bluff body followed by a second shedding from the opposite end. The way in which DMD can be used to deconvolve the second flow into symmetric and von Karman vortices is demonstrated.

The analyses performed illustrate two distinct advantages of DMD: (1) Unlike proper orthogonal modes, each dynamic mode is associated with a unique complex growth rate. By comparing DMD spectra from multiple nominally identical experiments, it is possible to identify "reproducible" modes in a flow. We also find that although most high-energy modes are reproducible, some are not common between experimental realizations; in the examples considered, energy fails to differentiate between reproducible and non-reproducible modes. Consequently, it may not be possible to differentiate reproducible and non-reproducible modes in POD. (2) Time-dependent coefficients of

dynamic modes are complex. Even in noisy experimental data, the dynamics of the phase of these coefficients (but not their magnitude) are highly regular. The phase represents the angular position of a rotating ring of cells and quantifies the downstream displacement of vortices in reacting flows. Thus, it is suggested that the dynamical characterizations of complex flows are best made through the phase dynamics of reproducible DMD modes.

---
* Corresponding Author: sroy@woh.rr.com

I. INTRODUCTION

Combustion instabilities can damage industrial systems severely and limit their performance [1, 2]. These instabilities are typically generated when a system is driven toward high performance or high efficiency and often take the form of uncharacteristically hot or cold spots [2–4]. Hot spots can cause extensive and irreparable damage in large chemical reactors [4], while cold patches can extinguish combustion in reactors or jet engines [5]. Prevention and control of the onset and growth of combustion instabilities is an important design goal.

A major difficulty with such a design is the lack of a sufficiently accurate and analytically or computationally solvable model system. Reacting flows can, in principle, be modeled using an appropriate system of reaction–diffusion equations [6–9], supplemented by the Navier–Stokes equations [10, 11]. However, several difficulties are involved. First, the precise details of the underlying chemical reactions and values for the diffusion rates of products are rarely known. Second, typical flows contain and are affected by long-range pressure and heat-release fluctuations. In particular, the zero-Mach-number (*i.e.,* fluid speed is much smaller than sound speed) assumption used in most analytical studies is not expected to be valid, even in simple configurations [12]. Third, the boundary conditions for most technologically relevant examples are non-trivial; consequently, special function expansions cannot be used to simplify the analyses. Computational analyses of reacting flows encounter difficulties as well. The nonlinearity of the underlying equations causes energy to be recursively cascaded from large scales to small scales; flow components on the resulting vastly different scales are coupled. Consequently, accurate simulation of a combustion flow requires that computations be performed on an extremely fine grid.

On the other hand, high-frequency, high-resolution imaging such as measurements of species-concentration fields through *planar laser-induced florescence* (PLIF) and of velocity fields through *particle-image velocimetry* (PIV), is feasible [13, 14]. The data can be used to perform modal decompositions and dimensional reductions of the flows. However, turbulent combustion contains reproducible and non-reproducible components. Random experimental and observational noise can only be quantified statistically. The small-scale "eddy-like" structures formed through energy cascading, while not "random," are not reproducible; they depend sensitively on the initial conditions from which they emerged. Only the

4

reproducible constituents can be used for flow characterization or control. Thus, successful post-processing of turbulent combustion should include techniques to deconvolve the flow into reproducible and non-reproducible constituents.

Nonlinear control methods that rely only on experimental data have been proposed [15, 16] and validated in contexts ranging from cardiac rhythms [17, 18] and laser systems [19] to neural signals [20, 21] and spatio-temporal fluid flows [22]. Specifically, the goal is to drive an irregular system toward an unstable periodic orbit [15, 23]. These periodic orbits are contained in the attractor; hence, the feedback necessary to implement control is small. More importantly, the periodic orbits and feedback can be computed from modal decomposition of data [22, 24]; no model of the underlying dynamical system is required.

Typically modal decomposition is implemented using a pre-specified basis expansion such as Fourier transforms or wavelets or, in the case of linear systems, through global eigenmodes [25, 26]. However, these approaches are not efficient in deconvolving nonlinear flows that are contained in irregular domains for two reasons: (1) the expansion of flow constituents such as eddies or vortices requires a very large number of modes [27], and (2) it is difficult to assign expansion modes to a specific flow constituent such as the von Karman vortices [13, 28]. *Proper orthogonal decomposition* (POD) addresses issue (1) [29–32]. First, there is no preconceived selection of the expansion modes; rather, the proper orthogonal modes are computed from data through a correlation matrix. Next, features of turbulent flows can be captured by $\sim$25 POD modes [13, 28]. The remaining modes are assumed to represent noise and non-reproducible features of the flow. However, in the examples studied below, it is not possible to use POD to resolve issue (2). (If the system is symmetric, it may be possible to associate symmetry-broken POD modes with symmetry-broken flow constituents [28].) It should be noted that POD is optimal in the sense that, at a given truncation, it provides the closest description of the original flow [32].

In this study we analyzed reacting flows using POD and an alternative decomposition based on *Koopman operator theory* [26, 33, 34], which generalizes eigendecomposition to nonlinear systems. Koopman modes are a generalization of normal modes [34], and each represents a global collective motion of the secondary field. The spectrum of the underlying dynamics (*e.g.,* reaction–dffusion and Navier–Stokes equations) is contained in the spectrum of the Koopman operator [26, 34]. Schmid [33] proposed a fast algorithm, referred to as *dynamic mode decomposition* (DMD), for computing approximately (a subset of) the

Koopman spectrum from the secondary field.

Two problems were studied. The first involves a cellular state formed on a flat circular flame front [5]. The state analyzed consists of two "rings" of cells that co-rotate at different rates. Proper orthogonal and dynamic mode decompositions were compared and contrasted. Both can be used to differentiate the dynamics associated with the two rings. However, multiple dynamic modes have the same spatial structure but different growth rates. They combine to form a single proper orthogonal mode. Thus, POD is the more parsimonious or efficient expansion, while DMD provides more refined dynamical details of the modes. The second problem involves reacting flows behind a symmetric bluff body. The flow contains two types of eddies–periodic shedding of symmetric pairs of vortices and von Karman shedding, where vortices are shed alternately from opposite sides of the bluff body. How POD and DMD can be used to differentiate the two types of vortex shedding is demonstrated.

In these studies, two features of DMD are identified that are extremely useful in deconvolving the flow. First, unlike proper orthogonal modes, each dynamic mode is associated with a unique complex growth rate. Comparing DMD spectra from multiple nominally identical experiments (or from different segments of the same experiment) aids in identifying "reproducible" modes in a flow. Spatio-temporal dynamics represented by the remaining modes presumably reflect noise and features sensitive to the precise initial conditions. In addition, as our analyses show, high-energy modes of the flow are typically, but not always, reproducible. This may also be be true in POD. Thus, we were unable to differentiate reproducible and non-reproducible modes in POD. The second issue involves the use of DMD to identify multiple modes contained in a single flow constituent. The time-dependent coefficients of the dynamic modes are complex functions. Even in noisy experimental data, we find that the phase of these coefficients (but not their magnitude) exhibits repeatable dynamics. The phase represents the angular position of a rotating ring of cells and quantifies the downstream displacement of the vortices in reacting flows. Whether two dynamic modes should be assigned to a single flow constituent can be determined using Lissajous figures. A flow constituent can be reconstructed when all DMD modes associated with it are known.

Proper orthogonal and dynamic mode decompositions are outlined in Section II. Section III introduces a state of two co-rotating rings of cells on a combustion front and reports results from POD and DMD. It was found that either decomposition can be used to partition the dynamics to those of the outer and inner rings of cells. POD and DMD are compared

6

using this example. The algorithm to capture noise and other non-reproducible features of the flow is introduced. In Section IV these ideas are employed to analyze vortex shedding behind a symmetric bluff body. Two types of flows are considered. In the first, symmetric vortex pairs are shed periodically from either side of the bluff body. In the second, von Karman vortices are also included. Proper orthogonal and dynamic mode decompositions are conducted on both classes of flows. In particular, DMD was used to differentiate the primary flow components from noise and other non-reproducible aspects of turbulent combustion and also to select modes with similar phase dynamics. Finally, in Section V the implications of the results are discussed. The Appendix outlines conditions under which combinations of dynamic modes can be a proper orthogonal mode.

II.   MODAL DECOMPOSITION

Below, we briefly outline dynamic mode and proper orthogonal decompositions and the associated computations from a spatio-temporal field. These presentations are included only for completeness and follow Refs. [26, 29–34]. Suppose the state of a system is $\mathbf{z}$ and its dynamics are given by

$$\dot{\mathbf{z}} = \mathcal{F}(\mathbf{z}), \tag{1}$$

with an appropriate set of boundary conditions. The dynamics evolve the initial state $\mathbf{z}_0$ of the system to $\mathbf{S}^t(\mathbf{z}_0)$ at time t. In the case of reacting flows, $\mathcal{F}$ consists of the relevant reaction–diffusion and Navier–Stokes equations with, perhaps, no-slip boundary conditions. For reacting flows, these equations and the associated model parameters along with the boundary conditions are not known with sufficient accuracy to make reliable predictions. On the other hand, one has available high-frequency, high-resolution data on various secondary fields associated with the flow; *e.g.,* the concentration field through PLIF or velocity field through PIV. Let us represent one such (observable) secondary field (associated with $\mathbf{z}$) by $u[\mathbf{z}](\mathbf{x})$, where $\mathbf{x}$ are the grid points on which the observations are made. As the state of the system evolves from $\mathbf{z}_0$ at time $t = 0$ to $\mathbf{S}^t(\mathbf{z}_0)$ at time t, the secondary field evolves from $u[\mathbf{z}_0](\mathbf{x})$ to $u\left[\mathbf{S}^t(\mathbf{z}_0)\right](\mathbf{x})$. When the context is clear, one can simplify the notation by writing $u(\mathbf{x}, t)$ for $u\left[\mathbf{S}^t(\mathbf{z}_0)\right](\mathbf{x})$.

A. Proper Orthogonal Decomposition

In POD $u(\mathbf{x}, t)$ is decomposed in a basis $\{\Psi_k(\mathbf{x})\}$ whose members are the normalized eigenvectors of the correlation matrix $\mathbf{C}$ given by $C_{\mathbf{x},\mathbf{x'}} \equiv \langle u(\mathbf{x}, t)u(\mathbf{x'}, t)\rangle_t$, where $\mathbf{x}$ and $\mathbf{x'}$ are two spatial locations, and the average is over time. Since $\mathbf{C}$ is real and symmetric, POD modes $\{\Psi_k(\mathbf{x})\}$ are real and orthogonal. $\Psi_0(\mathbf{x})$ is the time-averaged field. For fields in two spatial dimensions, denote the number of pixels in the two directions by H and W. The spatio-temporal field can be expanded as

$$u(\mathbf{x}, t) = \sum_{k=0}^{N-1} b_k(t)\Psi_k(\mathbf{x}), \tag{2}$$

where $N \leq HW$ is the number of POD modes, and $b_k(t)$ are the time-dependent coefficients.

Variations in $u(\mathbf{x}, t)$ can be quantified using $V \equiv \mathbb{E}\left[(u(\mathbf{x}, t))^2\right]$, where the expectation is over the grid points and snapshots. Using the expansion of $u(\mathbf{x}, t)$ and the orthonormality of $\Psi_k(\mathbf{x})$'s, one observes that $V = \sum\langle|b_k(t)|^2\rangle_t$. $L_k \equiv \langle|b_k(t)|^2\rangle_t$ can be interpreted as the contribution of the kth mode to V; it is referred to as the energy (or latency). The terms in the expansion are reordered so they are in a non-increasing order of L_k. Generally, it is assumed that high-energy modes are robust, and that the remaining ones represent noise and other irregular features of the flow. A reduced-order approximation [35] for the flow can be derived by truncating the series (2) at an appropriate order n ($< N$) to obtain $u_n(\mathbf{x}, t) \equiv \sum_{k=0}^{n-1} b_k(t)\Psi_k(\mathbf{x})$. The "quality" of the approximation is given by

$$\beta_n = \frac{\sum_{k=0}^{n-1} L_k}{\sum_{k=0}^{N-1} L_k}. \tag{3}$$

Larger values of β_n correspond to better approximations of the data. POD modes are the most efficient basis in the sense that for given n, no other decomposition of the form $\sum_{k=0}^{n-1} \tilde{b}_k(t)\tilde{\Psi}_k(\mathbf{x})$ has a larger value of β_n [29–32].

B. Dynamic Mode Decomposition

The Koopman operator is a linear operator U^t that maps the function $u(\mathbf{x}, t = 0)$ (the initial state) to the function $u(\mathbf{x}, t)$ [26, 34], *i.e.,*

$$U^t : u(\mathbf{x}, t = 0) \to u(\mathbf{x}, t). \tag{4}$$

8

U^t is assumed to depend on $\mathcal{F}$ and t. Unlike $\mathcal{F}$, which can be a nonlinear system, U^t is an infinite dimensional linear operator [34]. Its eigenfunctions are referred to as the *Koopman eigenfunctions*. Projections of the state $u(\mathbf{x}, t = 0)$ to the Koopman eigenfunctions are known as the *Koopman modes*. Interestingly, under very general conditions, the spectrum of $\mathcal{F}$ is contained in the spectrum of U^t [26, 34]; hence, the stability and structure of solutions $\mathbf{z}(t)$ of the system $\mathcal{F}$ can be inferred through the analysis of the Koopman operator.

Dynamic mode decomposition [25, 33, 36] is an efficient algorithm for computing approximations to the Koopman spectrum and Koopman modes from experimental snapshots collected at uniform time intervals δt. Since $U^{\delta t}$ is independent of the state $u(\mathbf{x}, t)$, one can approximate the transformation of the field during the time interval $[t, t + \delta t]$ as

$$u\left(\mathbf{x}, t + \delta t\right) \approx \mathbf{A} u\left(\mathbf{x}, t\right), \tag{5}$$

where $\mathbf{A} \equiv \mathbf{A}(\delta t)$ is a matrix of size $HW \times HW$. If one denotes by u_k the field corresponding to the snapshot taken at time $t = k\delta t$, Eqn. (5) can be re-written as $u_{k+1} \approx \mathbf{A} u_k$. Thus,

$$\mathbb{U}_1 \equiv [u_1, u_2, \ldots, u_n] \approx \mathbf{A}\left[u_0, u_1, u_2, \ldots, u_{n-1}\right] \equiv \mathbf{A}\mathbb{U}_0. \tag{6}$$

Finally, singular value decomposition of $\mathbb{U}_0 = \mathbf{V}\mathbf{S}\mathbf{W}^T$ can be used to compute the spectrum of $\mathbf{A}$ (or equivalently of $\mathbf{V}^T\mathbf{A}\mathbf{V}$) by noting that $\mathbf{V}^T\mathbf{A}\mathbf{V} = \mathbf{V}^T\mathbb{U}_1\mathbf{W}\mathbf{S}^{-1}$ [36]. Eigenfunctions of $\mathbf{A}$ are referred to as *dynamic modes* of the flow [25, 33, 36]. Dynamic mode decomposition provides an approximation to a subset of the Koopman spectrum Λ_n and the corresponding Koopman modes $\Phi_n(\mathbf{x})$. Koopman modes evolve as $\exp(\Lambda_n t)$ under $\mathcal{F}$.

It should be noted that since $\mathbf{A}$ is not symmetric, its eigenvalues Λ_n and the eigenfunctions $\Phi_n(\mathbf{x})$ are, in general, complex-valued. Furthermore, the eigenfunctions are not orthonormal. Eigenvalues of the Hermitian conjugate $\mathbf{A}^\dagger$ of $\mathbf{A}$ are $\Lambda_n^* t$. The corresponding eigenfunctions $\tilde{\Phi}_n(\mathbf{x})$ are orthogonal to $\Phi_n(\mathbf{x})$'s–specifically, with an appropriate normalization $\int d\mathbf{x} \, \tilde{\Phi}_m(\mathbf{x})\Phi_n(\mathbf{x}) = \delta_{mn}$.

The spatio-temporal field $u(\mathbf{x}, t)$ can be expanded as

$$u(\mathbf{x}, t) = \sum a_k(t)\Phi_k(\mathbf{x}), \tag{7}$$

where the sum is performed over the DMD modes. By the orthonormality introduced above, $a_k(t) = \int d\mathbf{x} \, \tilde{\Phi}_k(\mathbf{x})u(\mathbf{x}, t)$. If necessary, the field can also be expanded in the basis $\{\tilde{\Phi}(\mathbf{x})\}$ as $u(\mathbf{x}, t) = \sum \tilde{a}_k(t)\tilde{\Phi}_k(\mathbf{x})$. Now the variations in the spatio-temporal dynamics reduce to

$V = \sum a_k \tilde{a}_k$, and one can interpret the quantity $L_k = a_k \tilde{a}_k$ as the energy associated with the kth mode. Note, however, that because DMD modes are not orthogonal, L_k is not strictly positive; hence, in defining β_k [Eqn. (3)], one must sum absolute values. It should be noted, however, that with this definition, L_k may exceed 1, although no such examples were found in the studies reported here.

Unlike proper orthogonal modes, dynamic modes are associated with unique eigenvalues Λ_n. One can use the extra information to address an important issue. In typical complex flows, a single flow constituent (*e.g.,* von Karman vortices) may not be captured by a single proper orthogonal or dynamic mode [28]. In such cases, we know of no method in POD for identifying and assigning modes to a constituent. In contrast, analysis of simulated and experimental data suggests that the dynamic modes associated with a flow constituent can be identified. Specifically, such eigenvalues are found to lie on a smooth curve in the complex plane [25, 33, 36]. An alternative scheme is as follows: recall that the primary dynamic mode (*i.e.,* that with the highest energy) has a single frequency–the imaginary part of the corresponding Λ. One may expect dynamic modes with harmonics of this frequency to be associated with the same flow constituent. In the next section, these ideas are used to decompose cellular flame patterns and reacting flows behind bluff bodies.

DMD modes associated with reproducible features of a flow will be "robust," *i.e.,* they will be found in multiple realizations of an experiment. In contrast, modes representing non-reproducible flow characteristics will change with the realization. This observation leads to the following conjecture: *it is possible to differentiate reproducible and non-reproducible aspects of a flow by comparing DMD spectra from multiple realizations of a set of nominally identical experiments.* Finally, it was observed that in constructing reduced-order models, one can discard the non-reproducible features and retain only their statistical characteristics; in other words, one need to consider only the primary, robust flow constituents in reduced-order models.

III. CELLULAR FLAME PATTERNS

A. The Experiment

The experimental setup is discussed in Refs. [5, 27, 37] and shown schematically in Figure 1(a). Cellular flame patterns were generated on a circular porous-plug burner that was mounted in a combustion chamber, which was maintained at a pressure of $0.3 - 0.5$ atm. A mixture of methane and air entered a porous medium and, following passage through it, formed a flat flame front. The front was a luminous disk 5.62 cm in diameter and $\sim$0.5 mm thick. The ambient pressure, fuel/oxidizer ratio, and flow rate were controlled to within 1%. A Dage-MTI charge-coupled-device camera was mounted vertically on top of the combustion chamber to record the spatio-temporal patterns.
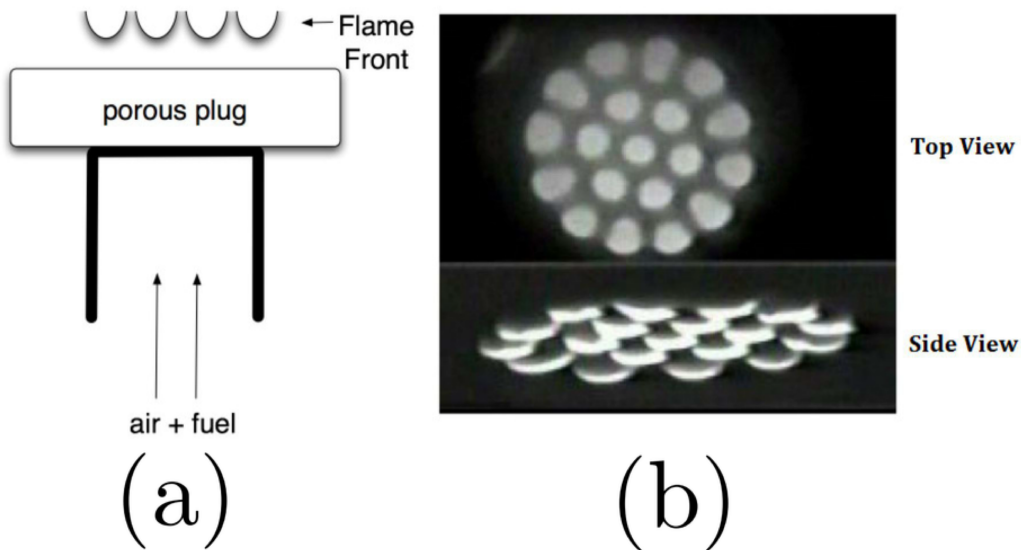
FIG. 1. (a) Schematic of the experimental setup generating cellular flames. (b) An example of a cellular state as observed from the top and the side. Notice that the darker (cooler) regions of the flame lie further from the porous plug.

As the flow rate was increased, the circular flame front experienced local curvature, resulting in symmetry-broken cellular structures such as those shown in Figure 1(b). The cellular pattern consisted of brighter (hotter) cells demarked by darker (cooler) cusps that extended farther away from the porous plug. The motion was video-recorded at 30 Hz. The spatio-temporal dynamics were captured by $N = 123$ equally spaced snapshots, with

11

a resolution of $W = 216$ pixels along the length and $H = 190$ pixels along the width of a snapshot. Both POD and DMD were implemented on a matrix of $W \times H$ columns (spatial points in a snapshot) and N rows (number of snapshots).

B. The Double Rotating State

A cellular flame pattern of two co-rotating rings of cells was analyzed, several consecutive snapshots of which are shown in Figure 2. The inner ring of two cells and the outer ring of six cells rotated clockwise, although at different rates. States where the rings rotated in opposite directions and those with rings containing different numbers of cells were also observed and described in Ref. [5]. The analysis outlined below has been applied to these patterns as well.

Frame 15 Frame 16 Frame 17 Frame 18
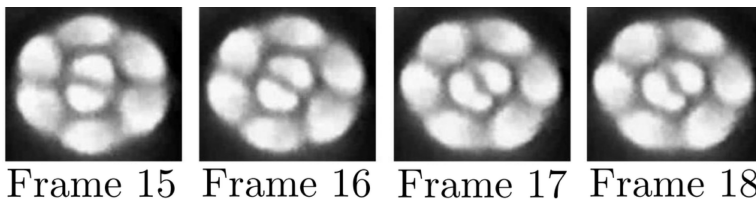
FIG. 2. Several consecutive snapshots from the cellular flame state of two co-rotating rings of cells. Both rings execute clockwise rotations, the angular speed of the inner ring being larger.

C. Proper Orthogonal Decomposition

Figure 3 shows the energies of the first sixteen proper orthogonal modes of the co-rotating cellular state, and Figures 4 and 5 show the first four proper orthogonal modes and the power spectra of their time-dependent coefficients. The first two modes have a six-fold symmetry and represent the outer ring, while the next two have a two-fold symmetry and are located near the inner ring. The next two modes (not shown) once again are located near the outer ring and have a twelve-fold symmetry. The fourth pair is located in the region of the inner ring and has a four-fold symmetry. In fact, the motion of a ring of k cells requires the coupling of modes of k and $2k$-fold symmetries, as discussed in Refs. [38, 39]. As seen from Panels (c) and (d) of Figures 4 and 5, the dynamics, $b_n(t)$, for these modes contain a narrow range of spectral components.
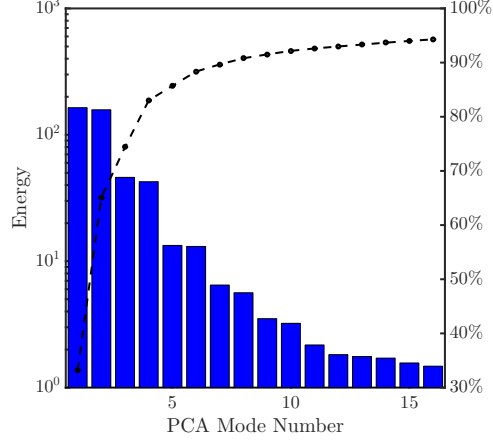
FIG. 3. Energies of the first 16 proper orthogonal modes of the double co-rotating state. Dashed line shows the cumulative energies as a fraction of the total, given in the scale at right. The mean mode $\Psi_0(\mathbf{x})$ has been removed.
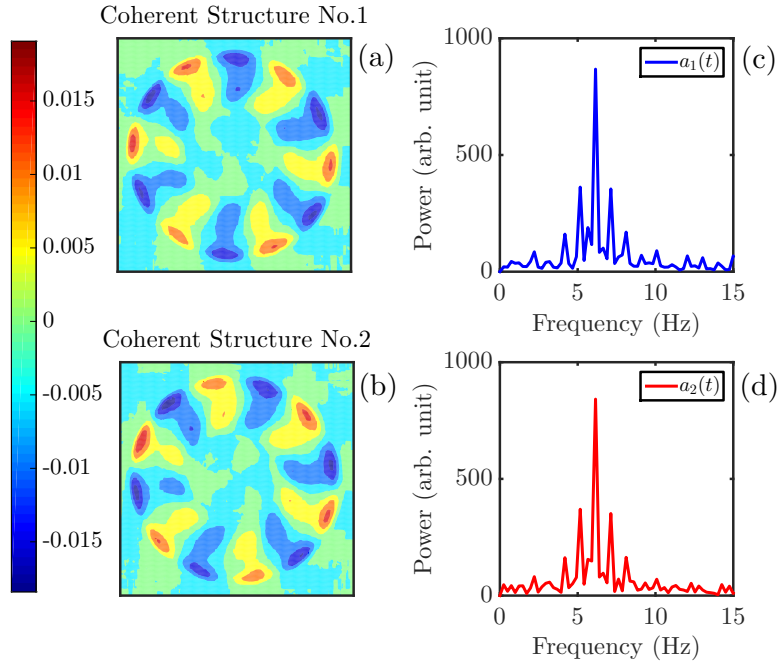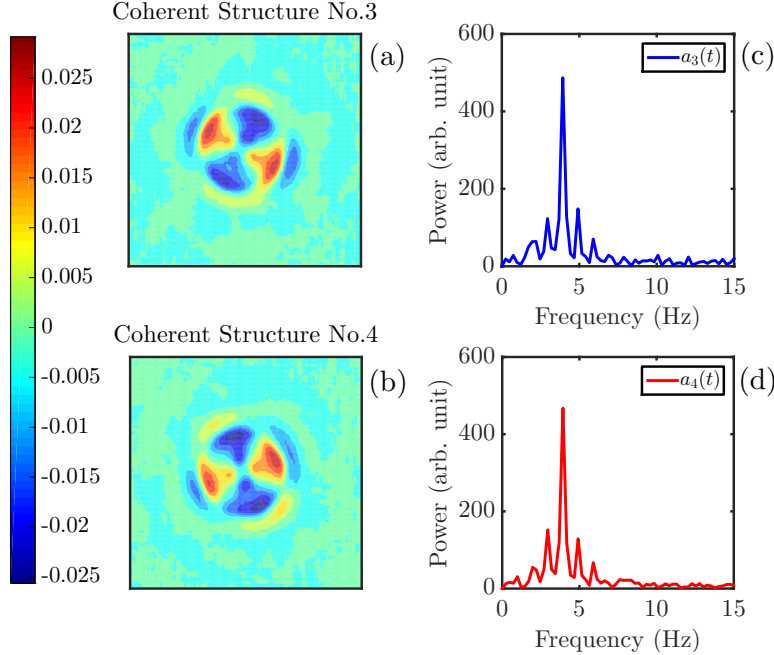

FIG. 4. (Color online) POD modes (a) $\Psi_1(\mathbf{x})$ and (b) $\Psi_2(\mathbf{x})$ and the power spectra of their time-dependent coefficients (c) $b_1(t)$ and (d) $b_2(t)$. Observe that the modes are located near the outer ring of cells. The power spectra in (c) and (d) have several significant Fourier components.

As Figure 3 shows, the first eight modes capture a significant fraction of the total energy of the spatio-temporal dynamics. The remaining modes are noisy, contain many small

13

FIG. 5. (Color online) POD modes (a) $\Psi_3(\mathbf{x})$ and (b) $\Psi_4(\mathbf{x})$ and the power spectra of their time-dependent coefficients (c) $b_3(t)$ and (d) $b_4(t)$. Observe that the modes are located near the inner ring of cells. The power spectra in (c) and (d) have several significant Fourier components.

scale irregular structures, and typically span the entire domain. Their energies decay very slowly, and they represent low energy states, noise, or non-reproducible features of the flame dynamics. The spatio-temporal dynamics of the *reproduction* (*i.e.,* the reduced-order dynamics) using the first $n = 9$ POD modes (including the 0th mode – mean of the spatio-temporal field over time) are

$$u_9(\mathbf{x}, t) = \sum_{k=0}^{8} b_k(t) \Psi_k(\mathbf{x}). \tag{8}$$

Figure 6 shows several snapshots of the approximation and should be compared with Figure 2. The differences between the two sets of snapshots are small. The spatio-temporal dynamics of the inner and outer rings can be extracted using reproductions that include modes $\{1, 2, 5, 6\}$ and $\{3, 4, 7, 8\}$, respectively, as also shown in Figure 6.

Although the spatio-temporal dynamics, $u_9(\mathbf{x}, t)$, are close to $u(\mathbf{x}, t)$, one cannot determine the roles played by the remaining POD modes (noise, finer features of the flow, etc.). Note also that the selection of POD modes 1, 2, 5, and 6 as belonging to a single flow constituent was based only on their symmetries.

14

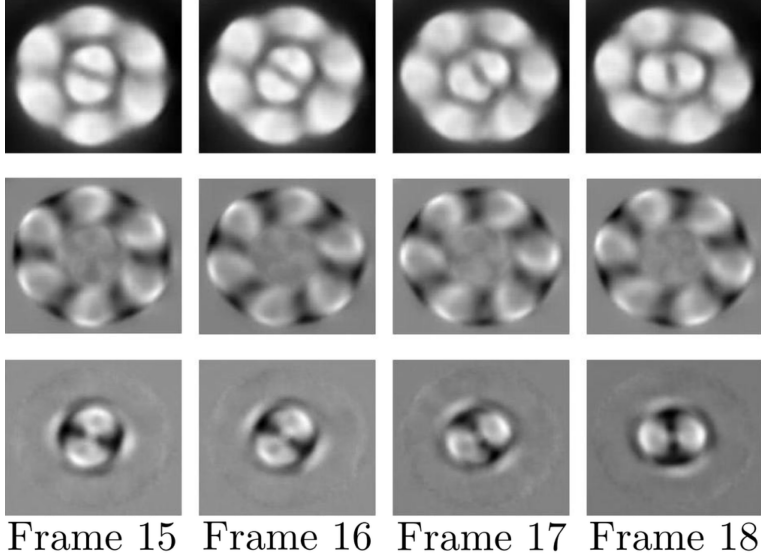Frame 15 Frame 16 Frame 17 Frame 18

FIG. 6. Reproductions of snapshots corresponding to those shown in Figure 2 are shown in the top row. The second and third rows contain reproductions of the outer and inner rings of cells. Both rings are moving clockwise, and the angular velocity of the inner ring is larger.
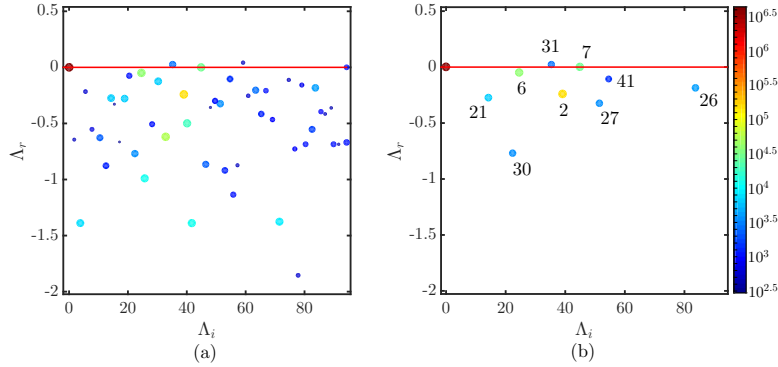
D. Dynamic Mode Decomposition

FIG. 7. (Color online) (a) DMD eigenmodes of the double co-rotating state with the 70 largest energies. Eigenmodes occur in complex conjugate pairs, and only those with non-negative real parts are shown. (b) Robust modes that remain unchanged –or nearly unchanged– between several sub-intervals of the dynamics. They are conjectured to represent reproducible features of the flow.

Figure 7(a) shows the (complex) eigenvalues of the dynamic modes for the double co-rotating state with the highest 70 energies. The modes appear in complex conjugate pairs

15

and only those with non-negative imaginary parts are shown. Next, the series of snapshots is subdivided into several subgroups, for example the first half, the second half, the middle half, etc. The DMD spectra for each of these subgroups are computed and a search initiated for the modes that are "robust", *i.e.,* those that are common to all subgroups. In our studies, the first consideration used is the proximity of the frequencies; specifically, if the imaginary parts between the subgroups differ by less than 3%. On the other hand, real parts of the eigenvalues are more variable; we suspect that this higher variability is related to that of the magnitude of $a_k(t)$ shown in Figure 10 below. We thus do not use them for our comparison. The next step is to verify that the modes have "similar" spatial structure. In cases where they have a well-defined spatial structure and/or symmetry (*e.g.,* Figures 4 and 5), these details can aid a comparison. A quantitative comparison is made as follows. Suppose we wish to determine if a (normalized) mode $\Phi(\mathbf{x})$ associated with the full set of snapshots can be identified with a (normalized) mode $\Phi^{(s)}(\mathbf{x})$ derived from a subgroup of the snapshots. Since the phases of the two DMD modes may differ, we first find a phase ϕ that minimizes the difference; *i.e.,* $\delta(s) \equiv min_\phi |e^{i\phi}\Phi(\mathbf{x}) - \Phi^{(s)}(\mathbf{x})|$. We then require that their maximum of $\delta(s)$ for different subgroups be smaller than a pre-specified cutoff η in order for the DMD mode to be considered robust. For the analysis here, we used $\eta = 0.5$.

Robust modes, along with the mode numbers placed in non-decreasing order of their energies, are shown in Figure 7(b). The energies of the modes are color coded (online version) according to the color bar shown at the right.

Figure 8 shows the energies of the dominant modes. As can be observed, although some robust modes have high energies, it is not possible to partition robust and non-robust modes of the double rotating state using energy alone. Our conjecture is that robust modes represent reproducible features of the combustion flow; conversely, modes that are not robust are associated with non-reproducible features including noise.

Figure 9 shows the real and imaginary parts of the (complex) DMD mode $\Phi_2(\mathbf{x})$ with the highest energy; its eigenvalue is $\Lambda_1 = -0.24 + 39.02i$. The mode is located on the outer ring of cells and has the same six-fold symmetry, and its frequency is $\Omega_2 = Im(\Lambda_2)/2\pi \approx$ 6.21 (*frame rate*). If the mode was an exact Koopman mode, $a_2(t) \sim \exp(\Lambda_2 t)$ [26]. However, we observe, in Figures 9 (c) and (d), that the spectrum contains a small but non-zero broad-band component. This is because DMD modes are only approximations to Koopman modes.
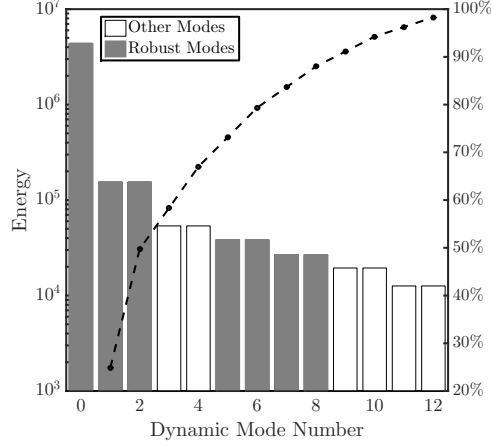
FIG. 8. Energies of the 12 dynamic modes with the largest energies. The robust modes are shown in gray. Dashed line shows the cumulative energies as a fraction of the total, given in the scale at right.
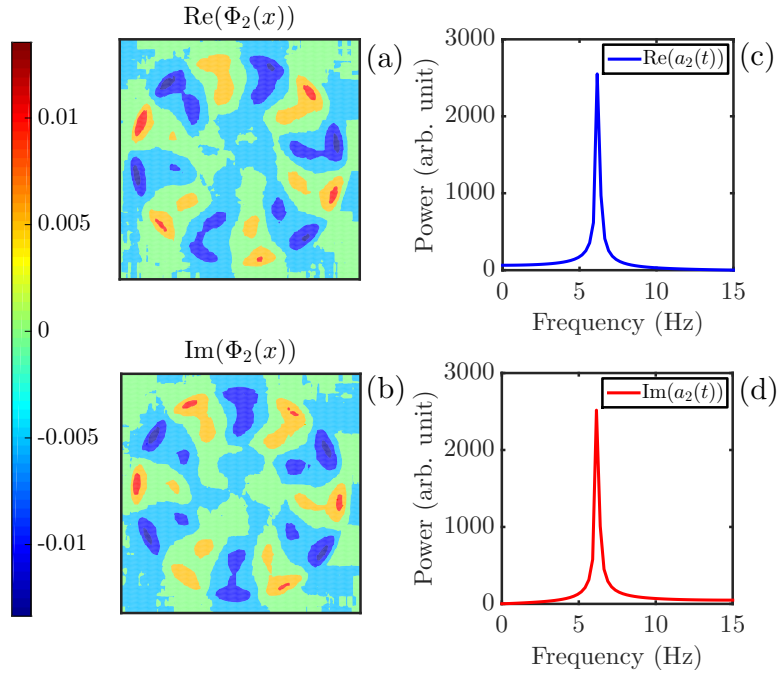

FIG. 9. (Color online) (a) Real and (b) imaginary parts of the dynamic mode of the double co-rotating state with the highest energy. The dynamics of the (c) real and (d) imaginary parts of $a_1(t)$ are dominated by the frequency Ω_1.

The coefficients $a_k(t)$ are calculated using Eqn. (7). The scatter plots of the real and

17
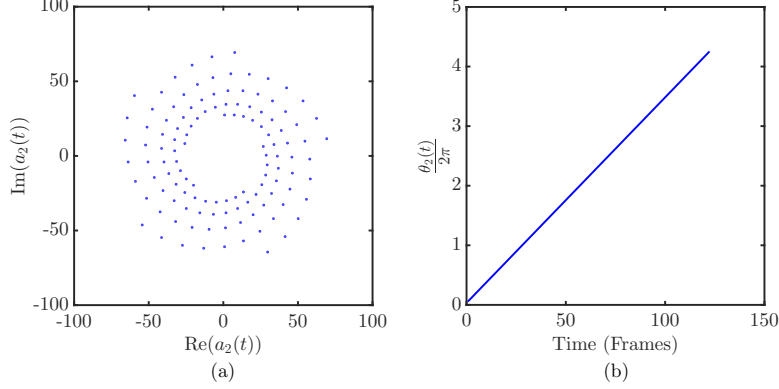
FIG. 10. (a) The points $a_2(t)$ in the complex plane are broadly distributed. However, the behavior of the phase angle, defined as $\theta_2(t) = tan^{-1} \left[Im(a_2(t))/Re(a_2(t)) \right]/s(2)$, where $s(2)$ is the symmetry of the mode, evolves smoothly. The slope $\omega_2(t)$ of the curve is the angular velocity of the ring.

imaginary parts of $a_2(t)$ are shown in Figure 10(a). Experimental noise, irregularities in the flow, and the cutoff used in the singular value decomposition (Section II B) cause fluctuations. Interestingly, the angular changes of the phase-space orbit are highly robust, and the irregularities are restricted to the radial component. To illustrate this point, we define

$$\theta_2(t) = tan^{-1} \left[Im(a_2(t))/Re(a_2(t)) \right]/s(2), \tag{9}$$

where $s(2)$ denotes the spatial symmetry of $\Phi_2(\mathbf{x})$; specifically, $\Phi_2(\mathbf{x})$ belongs to the dihedral group $D(s(2))$. Thus, $s = 2$ for the inner ring and $s = 6$ for the outer ring. The role of $s(2)$ in the definition is justified from the following observation: when a ring of cells rotates by $2\pi/s(2)$, the pattern is repeated, and $tan^{-1} \left[Im(a_2(t))/Re(a_2(t)) \right]$ has changed by 2π.

As Figure 10(b) shows, the evolution of $\theta_2(t)$ is highly regular; its slope $\omega_2 \equiv \partial\theta_2/\partial t$ is the angular velocity of the ring of cells. Henceforth, $\theta(t)$ and $\omega(t)$ will be used to characterize the evolution of each dynamic mode. Also note that since the POD modes are real, no such angular behavior can be defined for single modes. However, when the mode energies occur in pairs, it is possible to associate a phase to pairs of POD modes [27].

Figure 11 shows the real and imaginary parts of the dynamic mode with the next highest energy, $\Phi_6(\mathbf{x})$, the power spectrum of $a_6(t)$, and the phase dynamics, $\theta_6(t)$. [Note that $\Phi_2(\mathbf{x}) = \Phi_1^*(\mathbf{x})$ has the same energy as $\Phi_1(\mathbf{x})$; similarly $\Phi_5(\mathbf{x})$ and $\Phi_6(\mathbf{x})$ have the same energy.] $\Phi_5(\mathbf{x})$ represents the inner ring and $\omega_5(t)$ its angular velocity. Once again, note that the power spectrum has a smaller spectral range than that of the corresponding POD
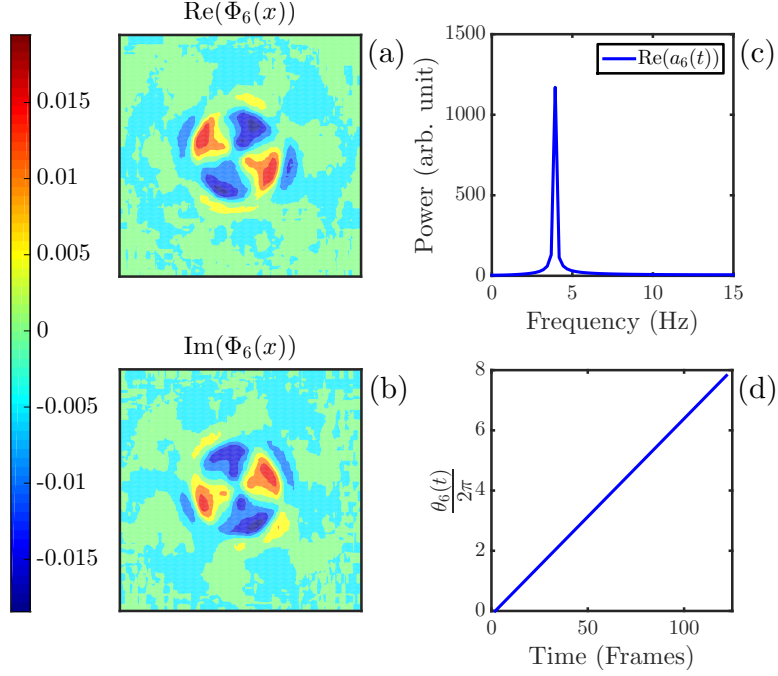
18

FIG. 11. (Color online) (a) Real and (b) imaginary parts of the robust dynamic mode of the double co-rotating state with the second highest energy. The dynamics of the (c) real part of $a_6(t)$ are dominated by one frequency. (d) The evolution of the phase of $a_6(t)$ is regular.

modes $\Psi_3(\mathbf{x})$ and $\Psi_4(\mathbf{x})$ and that the angular velocity of the inner ring is highly regular.

The spectrum of the dynamics of the DMD mode $\Phi_2(\mathbf{x})$ is different from those of the dynamics of the corresponding POD modes $\Psi_1(\mathbf{x})$ and $\Psi_2(\mathbf{x})$. An explanation of this observation follows. $\Phi_7(\mathbf{x})$ has a spatial structure that is a rotation of $\Phi_2(\mathbf{x})$; it is located in the outer ring and has the same six-fold symmetry. However, the eigenvalues Λ_2 and Λ_7 and the primary spectral components of $\hat{a}_2(\omega)$ and $\hat{a}_7(\omega)$ are different. In general, there can be multiple DMD modes with identical or symmetry-related spatial structure but with different eigenvalues. In POD such modes are combined into a single mode or a pair of modes such as $\Psi_1(\mathbf{x})$ and $\Psi_2(\mathbf{x})$. $\hat{b}_1(\omega)$ is the sum of the $\hat{a}(\omega)$'s for the associated dynamic modes. This is the sense in which the POD expansion is more efficient. However, even when multiple modes have the same spatial structure (*e.g.*, $\Phi_1(\mathbf{x})$ and $\Phi_7(\mathbf{x})$), DMD can be used to differentiate them through dynamics.

Finally, the relationship between different dynamic modes can be illustrated using Lissajous figures, such as Figure 12, which relate phases of a pair of modes through their Sine
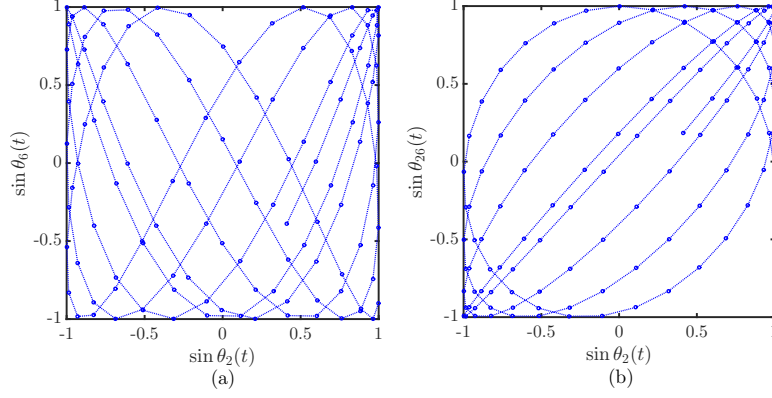
19

FIG. 12. (a) Plot of $\sin\theta_2(t)$ vs. $\sin\theta_6(t)$ showing that modes $\Phi_2(\mathbf{x})$ and $\Phi_6(\mathbf{x})$ exhibit independent dynamics. (b) In contrast, the angular velocities of modes $\Phi_2(\mathbf{x})$ and $\Phi_{26}(\mathbf{x})$ appear to be close, suggesting that they belong to a single flow constituent.

functions. Specifically, when the ratio of angular velocities for two phases θ_i and θ_j is a (low-order) rational number, pairs of points $\{\sin\theta_i(t), \sin\theta_j(t)\}$ lie on a curve. This is a helpful presentation of mode dynamics that may aid in identifying strongly coupled modes. For example, the dynamics of $a_2(t)$ appears to be uncorrelated with that of $a_6(t)$. On the other hand, angular velocities of $a_2(t)$ and $a_{26}(t)$ are nearly identical and the curve $(a_2(t), a_{26}(t))$ consist of nearly closed orbits. The lack of closure appears to be due to small shifts in the relative phase. We thus suspect that these modes are correlated. Such information is helpful in developing a low-order model for the flow.

Two significant advantages of dynamic mode decomposition are highlighted. First, the DMD spectrum from multiple, nominally identical experiments can be used to differentiate robust and non-robust aspects of a flow. We have not been able to identify a corresponding partition based on POD. Second, the dynamics of the phase defined in Eqn. (9), unlike the corresponding magnitude, exhibit very little noise. Hence, the phase dynamics, through Lissajous figures, can be used to search for modes that belong to the same flow constituent. In POD, an analogous phase can only be defined when pairs of proper orthogonal modes have identical energies [27].
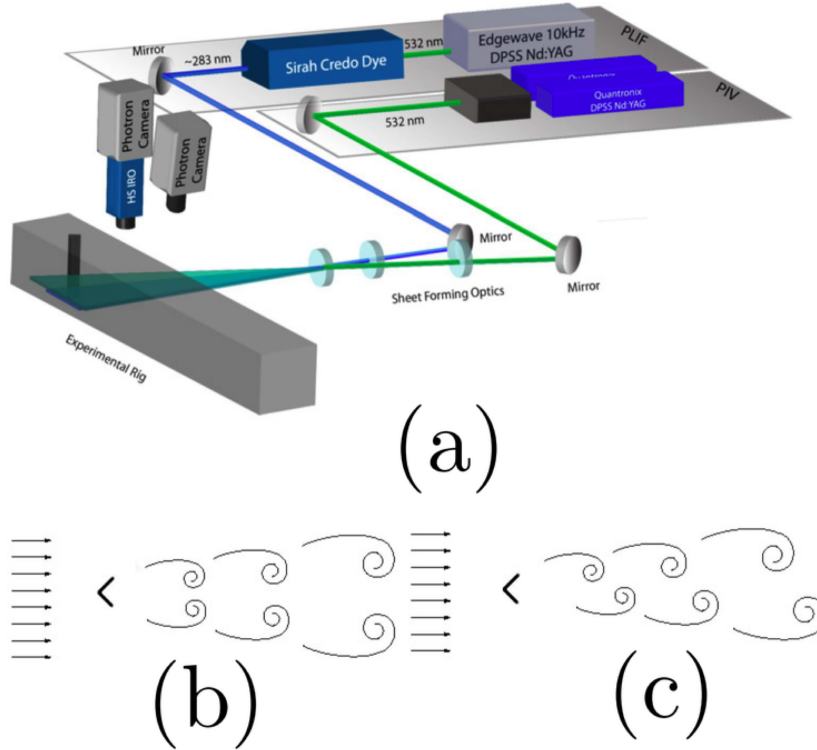
20

FIG. 13. (Color online) (a) Schematic of the reacting flow behind a v-gutter bluff body (adapted from [43]). Schematics showing (b) symmetric and (c) von Karman vortex shedding behind a symmetric barrier. Note that symmetric vortex shedding is not observed when the barrier has a circular cross-section.

IV. REACTING FLOWS BEHIND A BLUFF BODY

In this section, proper orthogonal and dynamic mode decompositions are used to analyze reacting flows behind symmetric bluff bodies. There are two classes of vortex shedding. The first, illustrated schematically in Figure 13(b), involves periodic shedding of symmetric pairs of vortices from either side of the bluff body. The second, shown in Figure 13(c), is von Karman shedding where a single vortex shed from one side of the bluff body is followed by another shed from the opposite side [10, 11]; von Karman shedding is periodic as well. Study of the onset and growth of vortex shedding behind bluff bodies is motivated partly by the changes in vortex dynamics as the equivalence ratio (*i.e.,* the fuel-to-oxidizer ratio and

the corresponding stoichiometric value) is changed from rich to lean conditions [13]. Vortex development must be constrained for controlling combustion instabilities related to various bluff-body combustors [6, 40].

A. The Experiment

Experiments on reacting flows were conducted within an optically accessible, atmospheric-pressure combustion test section that contains a bluff-body flame holder for flame stabilization. Air is delivered into a 152-mm × 127-mm rectangular test section at a constant rate of 0.32 kg/s. While the air rate is maintained constant, propane fuel is added and mixed upstream of the flame holder to provide equivalence ratios that vary between $\phi = 0.6$ and 1.1. The flame holder is a v-gutter with a width of 38.1 mm and an angle of 35°, which is capable of holding the flame to a blow-off equivalence ratio of $\phi = 0.55$. Additional facility details and flame-holder dimensions are provided in Ref. [13].

The bluff body is symmetric under reflection about a line parallel to the flow, and symmetric vortex shedding [41, 42] is observed in the entire range of control parameters. As the equivalence ratio is reduced, the flows develop, in addition, the asymmetric von Karman vortices [13].

A schematic of the experimental setup is shown in Figure 13(a), the details of which can be found in Ref. [43]. Two-dimensional images of hydroxyl (OH) behind the bluff-body v-gutter were acquired utilizing the PLIF technique. Briefly, PLIF of OH was performed using a 10-kHz, diode-pumped, solid-state Nd:YAG laser and a tunable dye laser. The 532-nm output of the Edgewave laser was used to pump the dye laser for obtaining tunable laser output at ∼586 nm. This wavelength was then frequency-doubled at ∼283 nm to excite the $Q_1(9)$ rovibrational transition in the $A^2\Sigma+ \rightarrow X^2\Pi$ $(1,0)$ band of OH. The $Q_1(9)$ transition has a low Boltzmann-fraction sensitivity between temperatures of 1000 and 2400 K, minimizing the need for a temperature correction on Boltzmann distributions when extracting flame fronts. The PLIF signal of OH was collected employing a LaVision dual-stage, high-speed UV intensifier (IRO) coupled to a Photron SA-5 CMOS camera. The collected light was filtered using a Brightline Semrock filter with ∼90% transmission between 300 and 340 nm. The combination of spectral filtering and time-gating of the intensifier allowed maximum fluorescence collection while minimizing interference from flame emission and laser scatter.

22

Fluctuations in the recorded PLIF intensity contained a uniform gradient in the y-direction, as verified by averaging several sets of snapshots. The effect can be observed in the snapshots shown in Figure 14 and in the POD and DMD modes, which are not symmetric quantitatively. If our studies had been limited only to spatial structures with a single symmetry type, we could have symmetrized the flow by replacing the experimental field with the average of all the symmtery-related fields. However, we wish to extract both the symmetric vortex shedding as well as time-delayed anti-symmetric von Karman vortex shedding from the same experiment; both features cannot be simultaneously symmetrized.
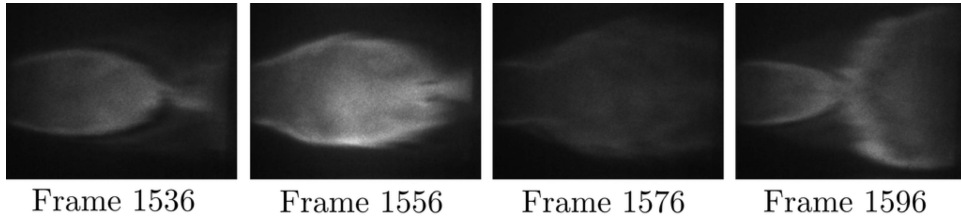
B. Symmetric Vortex Shedding

Frame 1536   Frame 1556   Frame 1576   Frame 1596

FIG. 14. Four snapshots of the reacting flow at $\phi = 1.1$, exhibiting symmetric vortex shedding of period $\sim$80 frames. Although the flow is expected to be symmetric, the PLIF images of these modes are not quantitatively symmetric as a result of a uniform gradient in the y-direction of the PLIF measurement.

In this section results are presented from POD and DMD of reacting flows behind the v-gutter bluff body that exhibit only periodic shedding of symmetric pairs of vortices. The flow is observed for equivalence ratios between $\phi = 0.9$ and $\phi = 1.1$. Figure 14 shows several snapshots of the vortex shedding at $\phi = 1.1$, displaying a period of $\sim$8 ms (80 frames). POD and DMD analyses were conducted on the last 4,000 of the 8,000 snapshots.

1. Proper Orthogonal Decomposition

Figure 15 shows the first two proper orthogonal modes and the power spectrum of their coefficients. The modes contain a single high-intensity patch (yellow/red) along the x-direction. These and all other relevant modes are (qualitatively) symmetric about a horizontal axis.

23

However, as mentioned earlier, the PLIF intensity displays a uniform gradient in the y-direction, which is reflected in the quantitative asymmetry of the proper orthogonal modes. The time-dependent coefficients of these modes exhibit a unique frequency of 120 Hz.
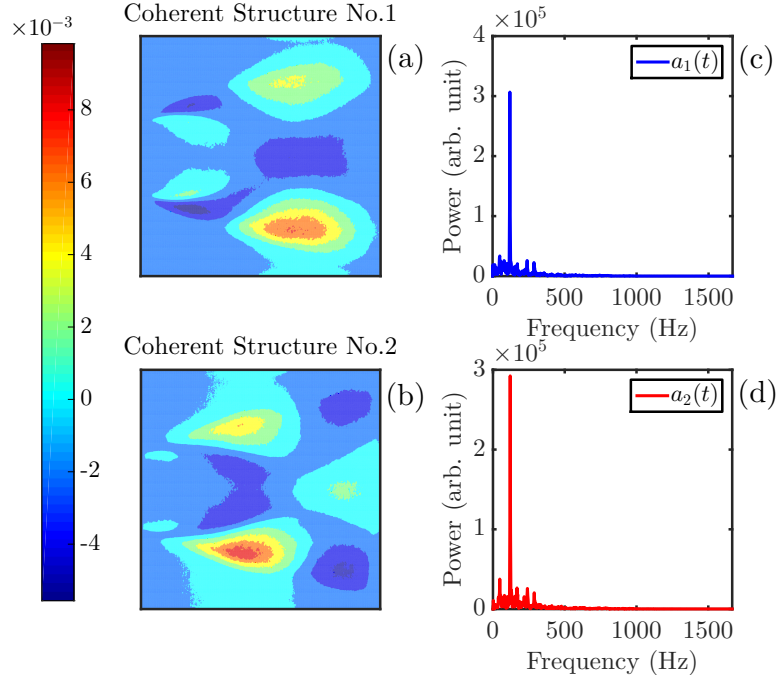

FIG. 15. (Color online) First (a) and second (b) POD modes for the reacting flow at equivalence ratio $\phi = 1.1$ where symmetric pairs of vortices are shed from the sides of the bluff body periodically. All primary POD modes are nearly symmetric for this flow. Power spectra of the time-dependent coefficients of these modes, shown in (c) and (d), exhibit a dominant frequency of 120 Hz.

The pair of POD modes with the next highest energies are harmonics; specifically, they contain two sets of high-intensity regions along the x-direction (compared to one in Figure 15), and the dominant spectral component of $\hat{b}_3(\omega)$ and $\hat{b}_4(\omega)$ is at a frequency of 240 Hz. Modes that represent higher harmonics of $\Psi_1(\mathbf{x})$ and $\Psi_2(\mathbf{x})$ are found as well.

2. Dynamic Mode Decomposition

Figure 16(a) shows the DMD modes and Figure 16(b) the robust modes, which are identified using 2000-frame sections of the video. The real parts of the robust modes vary between the subgroups and we show the mean and standard deviation for each robust mode. It should be noted that, following transient motions the system dynamics lies on an attractor,
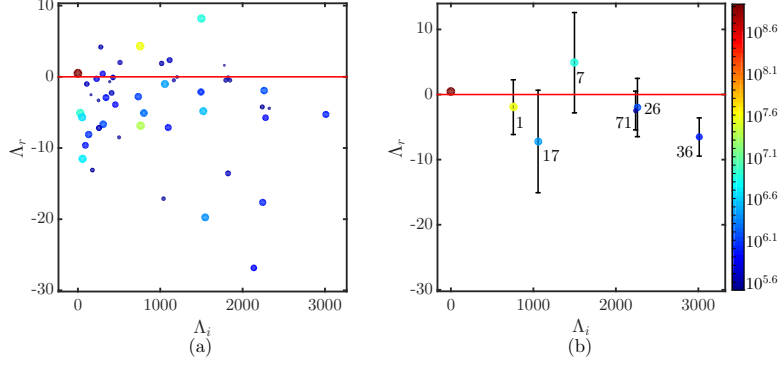
24

FIG. 16. (Color online) (a) DMD spectrum for the reacting flow at equivalence ratio $\phi = 1.1$. (b) The mean and standard deviation (for the real part) of robust DMD modes. The mode numbering is assigned according to the (non-increasing order of) energies.

and thus these real parts of the corresponding dynamic modes are expected to be zero [26, 34]. All error bars of robust modes in Figure 16(b) cross the real axis, suggesting that these modes are associated with motion on the attractor. The mode numbers in Figure 16(b) are ordered according to their energies shown in Figure 17. Once again most, but not all, of the high-energy modes are reproducible. This is another example to illustrate that energy does not partition robust and non-robust modes.
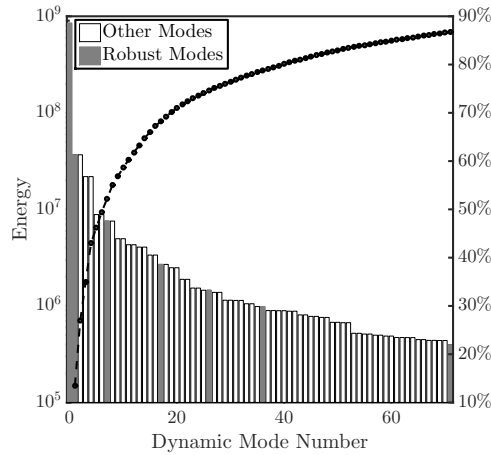

FIG. 17. Energies of the first 71 dynamic modes of the reacting flow at equivalence ratio $\phi = 1.1$. Robust modes are shown in gray. Dashed line shows the cumulative energies as a fraction of the total, given in the scale at right.

Figures 18(a) and (b) show the real and imaginary parts of the dynamic mode $\Phi_1(\mathbf{x})$.

Apart from the y-gradient in the PLIF field, the mode is symmetric about the x-axis. The coefficient of $\Phi_1(\mathbf{x})$, $a_1(t)$, has a dominant frequency of 120 Hz as seen in Figure 18(c). Furthermore, note that $\Phi_1(\mathbf{x})$ contains a single high-intensity (yellow/red) region along the x-direction [in contrast to $\Phi_7(\mathbf{x})$, see below]; one can define $s(1) = 1$, analogous to the symmetry of dynamic modes of the double-rotating state. However, here the definition pertains to the number of "structures" in the flow direction. As in the last section, a "phase" associated with the mode can be defined by $\theta_1(t) = tan^{-1}\left[Im(a_1(t))/Re(a_1(t))\right]/s(1)$. It represents the displacement of the structure along the x-direction rather than a spatial rotation in the previous example. One can also define $\omega_1(t) = \partial\theta_1(t)/\partial t$, which will be the flow velocity of the corresponding constituent. Figure 18(d) shows that the evolution of $\theta_1(t)$ is highly regular, in contrast to the noisy radial component $|a_1(t)|$. Thus, even though a significant variability exists between successive vortices, the fluctuations are in the magnitude of the coefficient [similar to Figure 10(a)]; the downstream flow velocity is highly regular.
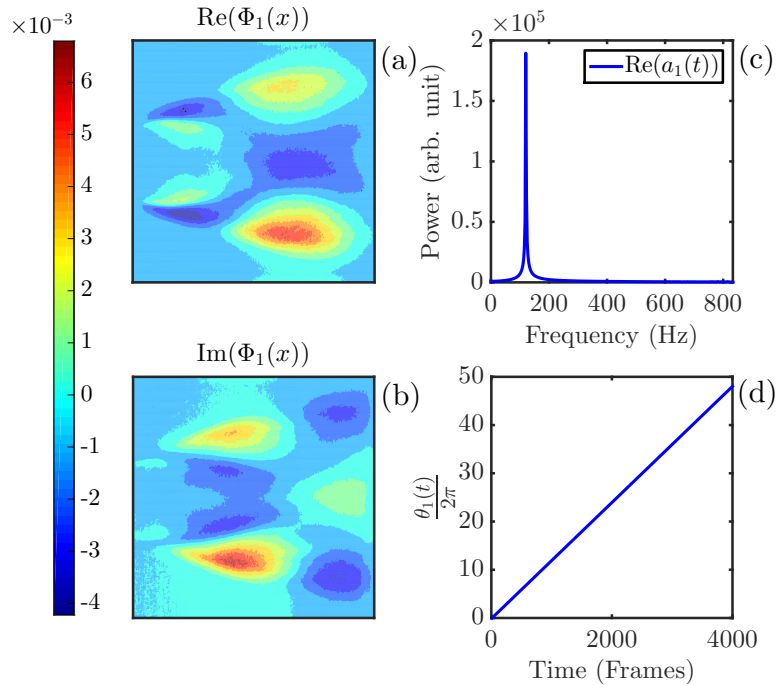

FIG. 18. (Color online) (a) Real and (b) imaginary parts of $\Phi_1(\mathbf{x})$ for the reacting flow at equivalence ratio $\phi = 1.1$. (c) The spectrum of $a_1(t)$ exhibits a dominant frequency at 125 Hz. (d) $\theta_1(t)$ exhibits smooth dynamics.

Figure 19 shows the real and imaginary parts of $\Phi_7(\mathbf{x})$, one of the two dynamic modes

with the next highest energy, and the Fourier transform of the real part of $a_7(t)$. $\Phi_7(\mathbf{x})$ contains two distinct high-intensity regions along the x-direction (those shown in yellow/red) and, thus, $s(7) = 2$. The phase has characteristics of a spatial harmonic of $\Phi_1(\mathbf{x})$, and the dominant frequency of $a_7(t)$ is 240 Hz. The dynamics of the phase $\theta_7(t)$, shown in Figure 19(d) are regular. Its angular velocity, ω_7 is identical to ω_1.
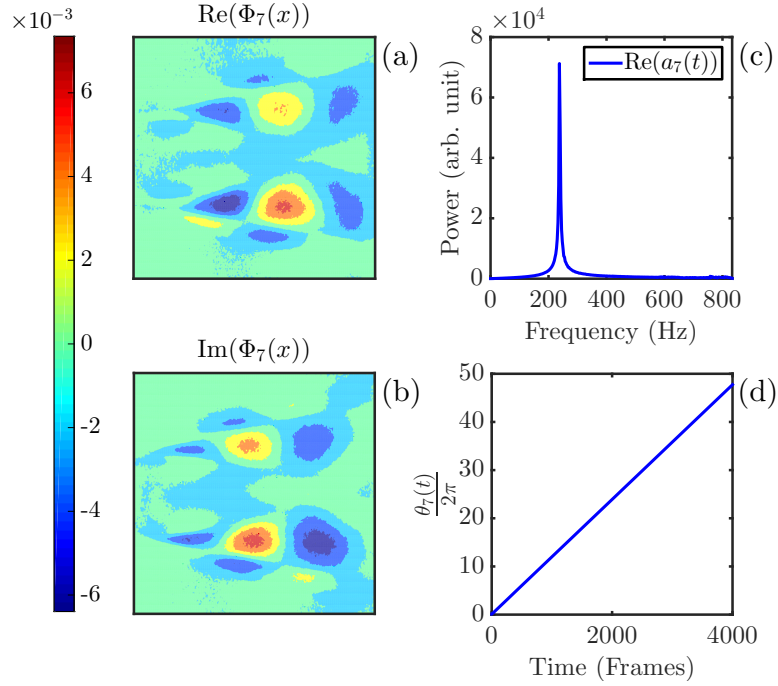

FIG. 19. (Color online) (a) Real and (b) imaginary parts of $\Phi_7(\mathbf{x})$ for the reacting flow at equivalence ratio $\phi = 1.1$. (c) $\hat{a}_7(\omega)$ peaks at 240 Hz. (d) $\theta_7(t)$ exhibits regular behavior, and the rate of its growth is identical to that of $\theta_1(t)$.

Interestingly, downstream flow rates of robust modes 1, 7, 26, 36 of the reacting flow at $\phi = 1.1$ are identical, as shown in Figure 20. (The figure only shows one from each of the four complex conjugate pairs of robust dynamic modes.) This observation suggests that the reacting flow at equivalence ratio $\phi = 1.1$ contains one reproducible flow constituent, which can be reconstructed using the eight robust modes and the time average $\Phi_0(\mathbf{x})$. Figure 21 shows several snapshots of this reconstruction; it should be compared with the corresponding images of the original flow shown in Figure 14.
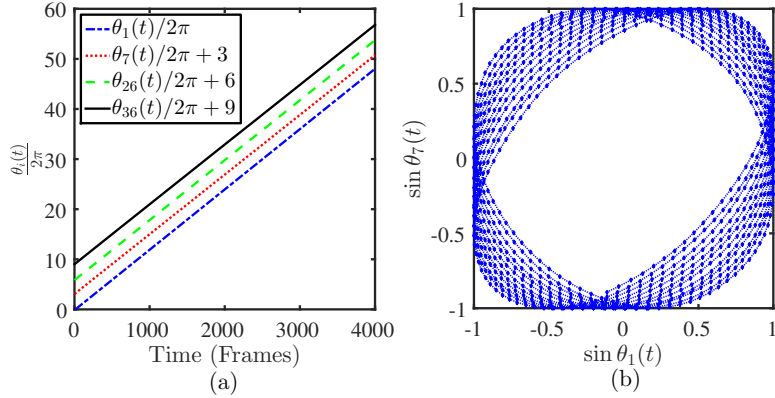
27

FIG. 20. (Color online) Phase growth of robust modes 1, 7, 26, 36 for the reacting flow at $\phi = 1.1$ are nearly identical. Successive curves are shifted for clarity. (b) The Lissajous figure for the last 1000 snapshots shows that Modes 1 and 7 are correlated, although some random drift between the phases is observed.

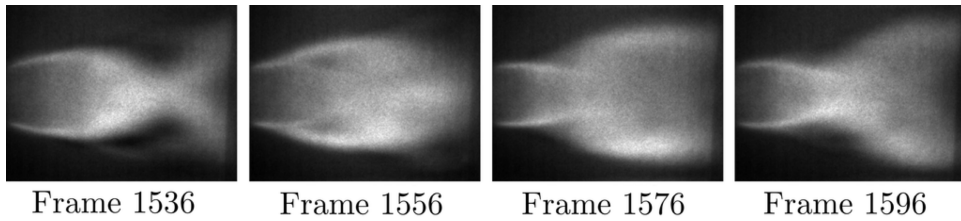Frame 1536   Frame 1556   Frame 1576   Frame 1596

FIG. 21. Several snapshots of the reconstruction of the reproducible flow using the robust modes. These snapshots should be compared with the corresponding snapshots of the original flow given in Figure 14.

C. Von Karman Vortex Shedding

The reacting flow at equivalence ratio $\phi = 0.8$ contains symmetric vortex shedding as well as von Karman shedding. Here noise and non-reproducible features of the flow are significantly higher than at $\phi = 1.1$. Part of this irregularity may be a consequence of the nonlinear coupling between symmetric and von Karman vortex shedding.

The flow contains both symmetric and asymmetric POD modes [13, 28], the leading modes being symmetric. As discussed in Ref. [28], the asymmetric modes must be associated with von Karman vortex shedding. Figure 22 shows the symmetric and asymmetric modes with

the highest energies.

Coherent Structure No.1   Coherent Structure No.7

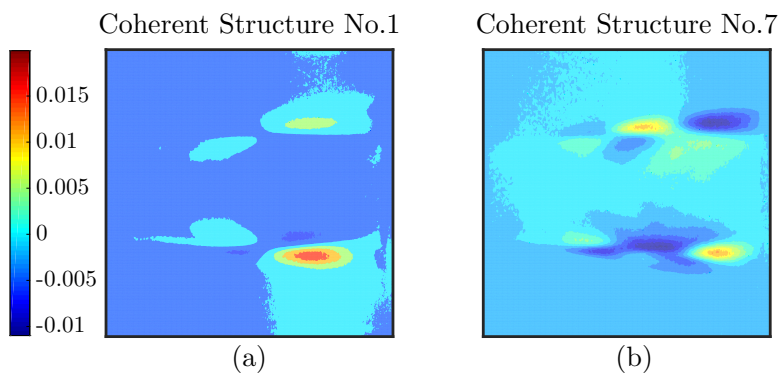(a)   (b)

FIG. 22. (Color online) (a) Symmetric and (b) asymmetric proper orthogonal modes with largest energies for the reacting flow at $\phi = 0.8$. The asymmetric modes represent von Karman vortex shedding [13, 28].

Figure 23(a) shows the DMD modes of the flow at $\phi = 0.8$, and Figure 23(b) shows the robust modes that were identified using 2000-frame sections of the flow.
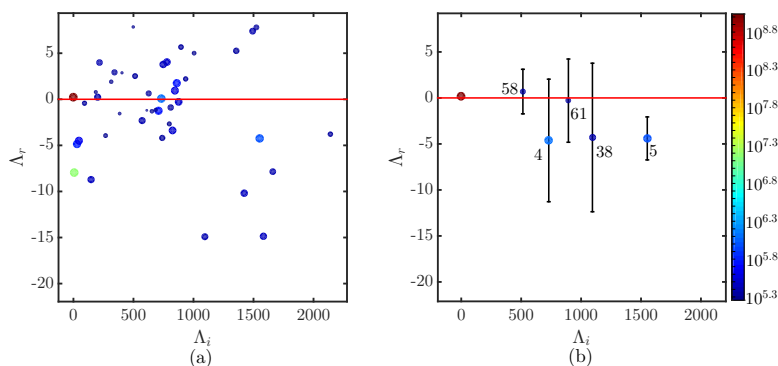

FIG. 23. (Color online) (a) The DMD spectrum for the reacting flow at equivalence ratio $\phi = 0.8$. The flow exhibits symmetric vortex shedding as well as von Karman shedding at this equivalence ratio. (b) The mean and standard deviation for the robust modes 4, 5, 38, 58, and 61.

Modes 4, 5, 38, 58, and 61 are robust. Modes 4 and 5 and symmetric about the x-axis, and mode 38 shows a von Karman-like behavior. Figure 24 shows the real and imaginary parts of $\Phi_4(\mathbf{x})$, the spectrum $\hat{a}_4(\omega)$ of the real part of $a_4(t)$, and the phase dynamics. The corresponding results for the asymmetric mode with the highest energy, $\Phi_{38}(\mathbf{x})$, are shown in Figure 25.
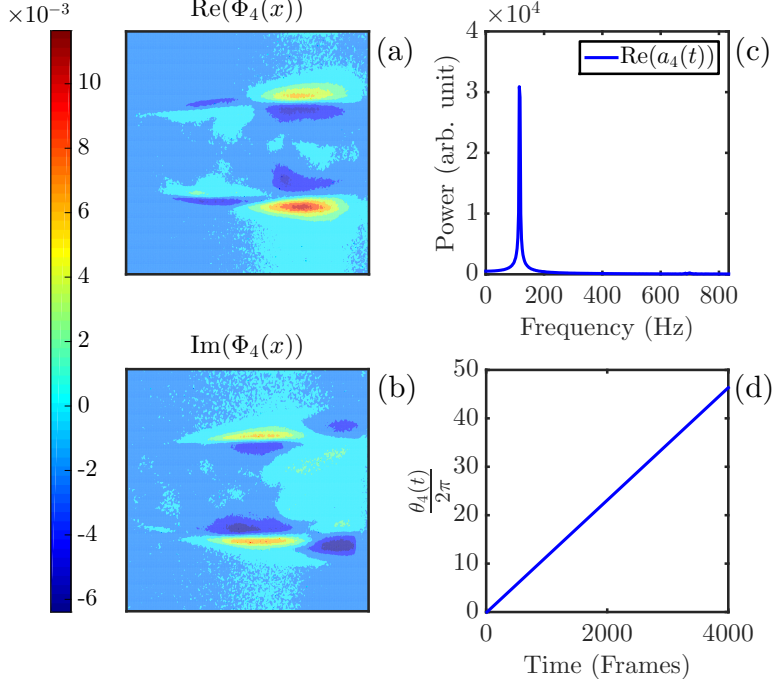
29

FIG. 24. (Color online) (a) Real and (b) imaginary parts of $\Phi_4(\mathbf{x})$, the symmetric mode with the largest energy, for the reacting flow at $\phi = 0.8$. (c) $\hat{a}_4(\omega)$ is significantly noisier than the corresponding spectra at $\phi = 1.1$; it contains a peak at 115 Hz. (d) phase dynamics of $a_4(t)$ are regular.

The phase dynamics of these five modes are significantly more regular (and noise-free) than the overall dynamics, as shown in Figure 26(a). The angular velocities $\omega_4(t)$ and $\omega_5(t)$ are approximately 0.073 and 0.078 radians/frame respectively, suggesting that they belong to a single flow constituent. The angular velocities ω_{38} and $\omega_{58}(t)$ are approximately 0.055 and 0.051 radians/frame, suggesting that they belong to a second flow constituent. However, the difference in angular velocities between the two pairs of modes (and the symmetry of the first pair and asymmetry of the second pair) implies that the two constituents are distinct. The reproduction of the flow using Φ_{38} shows that the constituent represents von Karman vortex shedding. The difference between the downstream flow rates of the symmetric and von Karman vortices means that the overall shedding is not periodic. That the two constituents are uncorrelated is reinforced by the Lissajous figure shown in Figure 26(b).

The top row of Figure 27 contains several snapshots from the reacting flow at $\phi = 0.8$. The next two rows show reconstructions of the symmetric and asymmetric constituents
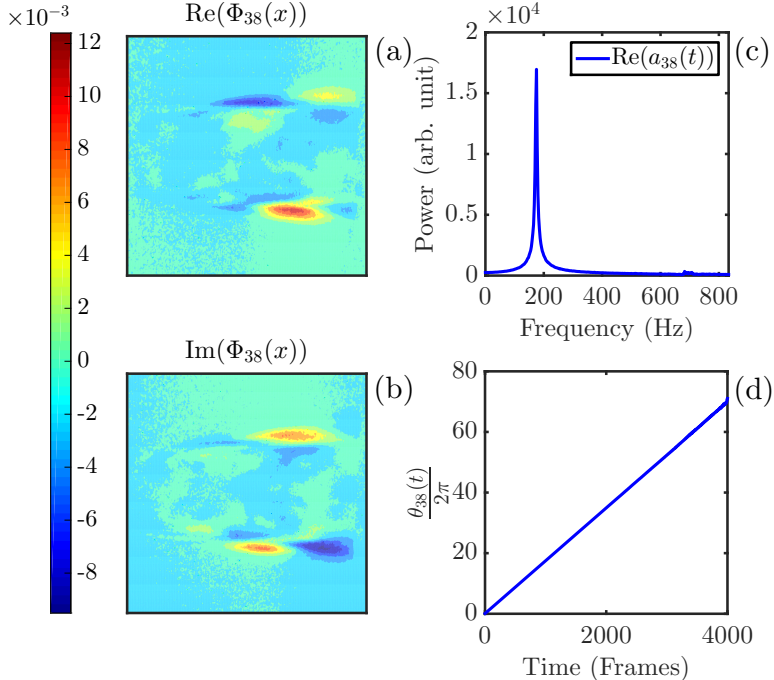
30

FIG. 25. (Color online) (a) Real and (b) imaginary parts of $\Phi_{38}(\mathbf{x})$, the asymmetric mode with the largest energy, for the reacting flow at $\phi = 0.8$. (c) $\hat{a}_{38}(\omega)$ is noisy with a peak at 175 Hz. (d) phase dynamics of $a_{38}(t)$ are regular.

at the corresponding time points. These can be interpreted as symmetric and von Karman vortex shedding. Here, evidence is found for the success of using DMD in separating the flow into distinct constituents. The symmetries of the constituents and the properties of their dynamics (for example, that the angular velocities are not identical) provide the information that is essential in the development of a low-dimensional model for the flow.

V. CONCLUSION

Recent advances in high-frequency, high-resolution imaging provide a strategy for analyzing complex flows [26, 34]. The goal is to identify distinct flow constituents and determine the coupling between them. However, experimental flows contain noise and, especially in the case of turbulent convection, features that are not reproducible; only their statistical properties are relevant. Thus, it is important to be able to differentiate reproducible features of the flow from noise and non-reproducible aspects. Once reproducible flow constituents
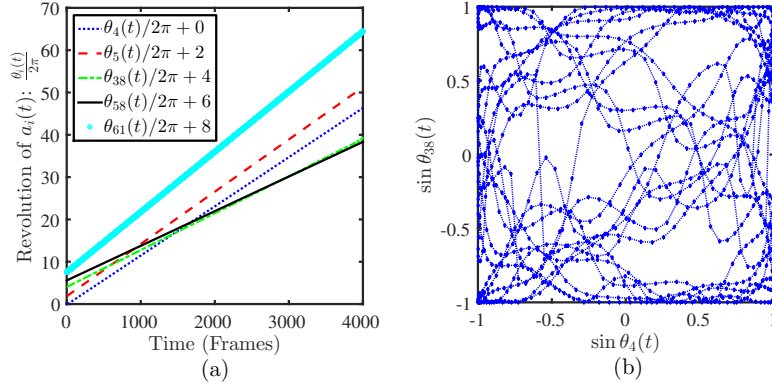
FIG. 26. (Color online) (a) Phase dynamics of several modes for the reacting flow at $\phi = 0.8$. "Angular velocities" $\omega_4 \approx 0.073$ radians/frame and $\omega_5 \approx 0.078$ radians/frame are nearly identical, suggesting that they belong to the same flow constituent. Similarly, $\omega_{38} \approx 0.055$ radian/frame and $\omega_{58} \approx 0.051$ radians/frame are close, suggesting that they form a second constituent. Successive curves are shifted for clarity. (b) The Lissajous figure for the last 1000 snapshots shows that Modes 4 and 38 are uncorrelated, underscoring that they belong to different flow constituents.
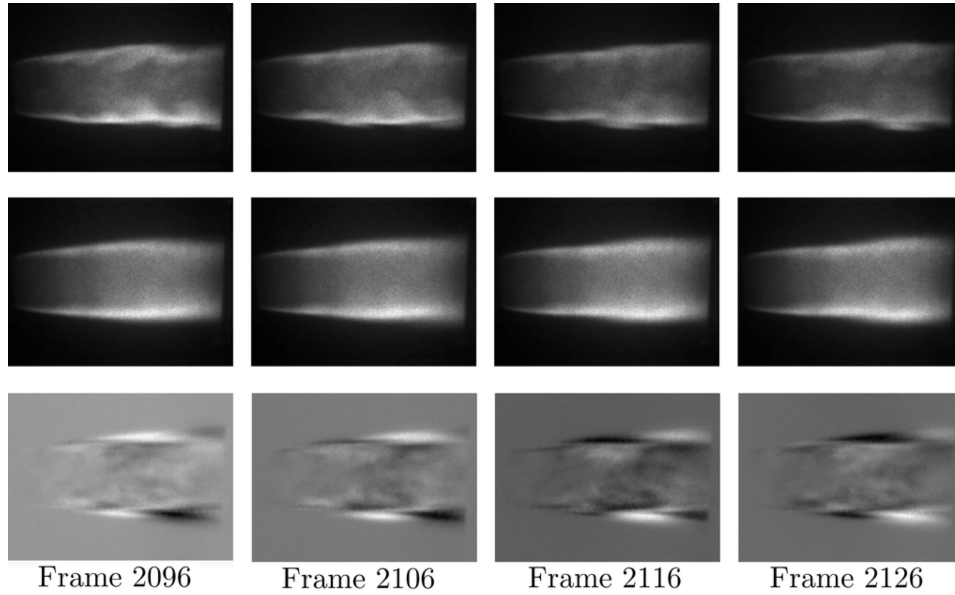

FIG. 27. Several snapshots of the reacting flow at $\phi = 0.8$ (top row), reconstructions of the symmetric (second row), and asymmetric (bottom row) flow constituents.

are identified, it is possible to introduce a low-order model of the flow.

The first step in the analysis is a modal decomposition of the flow. Since most real com-

bustors do not have symmetric regular shapes, the use of pre-specified bases such as Fourier or wavelet bases for post-processing is inefficient. Approaches such as POD, which extract the optimal basis functions from data, can be expected to be more effective. Indeed, the structure and dynamics of eddies in turbulent combustion can be captured with a (relatively) small number of proper orthogonal modes [13, 28]. However, it often is not possible to identify the set of POD modes to be associated with a specific flow constituent, such as a periodically shed collection of von Karman vortices.

In this study the use of dynamic modes was proposed to deconvolve combustion flows. DMD eigenvalues and eigenmodes can be computed from a series of equally spaced snapshots of the flow field. All spectral components of the dynamics underlying the flow are contained in the DMD spectrum [26, 33, 34]. Each DMD mode is associated with a single complex growth rate Λ. As in POD the relative importance of a mode toward the reconstruction of the spatio-temporal dynamics can be estimated using an appropriately defined energy.

Two reacting flows were analyzed using POD and DMD. The first was a non-trivial cellular state observed in a uniform circular flame front. A symmetry-breaking bifurcation of a uniform circular flame front generates a variety of stationary and non-stationary cellular states of the flame [5, 27, 37]. The state studied contained two rotating rings of cells that co-rotated with different angular speeds. The second set of flows analyzed was reacting flow behind symmetric bluff bodies [13, 41, 42]. In the first example, the flow contained only periodic shedding of symmetric pairs of vortices from the ends of the bluff body. In the second example, the flow contained symmetric and von Karman vortex shedding. The goal in both studies was to deconvolve the flow into its constituents and to differentiate them from noise and other irregular features.

Both POD and DMD can be used to separate the two rings of cells of the co-rotating cellular state. The constituents exhibited the expected symmetries and contained harmonics that are required for the rotation of rings [38, 39]. POD was the more efficient decomposition in the sense that the spatio-temporal dynamics were approximated with the smaller number of POD modes. In contrast, several dynamic modes had the same spatial structure but different growth rates. Thus, DMD presented more detailed dynamical descriptions of the modes.

A method to differentiate reproducible flow constituents from noise and non-reproducible features of the co-rotating cellular state was introduced. It is based on DMD of several

subsections of the flow and in identifying common eigenvalues. It was conjectured that these robust modes capture the reproducible features of the dynamics, and conversely, that non-robust modes represent non-reproducible features of the flow. (Ref. [44] introduces an approach to compute dynamic modes using multiple, nominally identical data sets. We expect that the selection of robust modes can be improved by using different combinations of the experiments.) It should be noted that we were not able to use POD for differentiating robust and non-robust modes in the examples we studied. First, as discussed in Section III D, the POD modes are a combination of DMD modes with the same spatial structure, and the contribution of the individual components (some of which may be reproducible, while others may not be) cannot be established. Second, we found that some non-robust DMD modes have higher energy than other robust DMD modes. One may suspect that the same holds for POD modes as well. Hence, it may not be possible to partition robust and non-robust modes based on the energies of POD modes alone. The ability to differentiate between robust and non-robust modes was a significant advantage of DMD over POD in post-processing our experimental data.

It was discovered that although the phase-space orbits are noisy, the angular motion (defined via the coefficients of DMD modes) associated with the states evolved with highly regular dynamics. This result suggests the use of the phase angle to describe the underlying dynamics and to identify strongly correlated pairs of modes through Lissajous figures. The rate of change of the phase angle was equal to the angular velocity of the corresponding ring of cells. Finally, a correlated group of dynamic modes can be used to reconstruct a flow constituent. It should be noted that, unless the POD modes can be paired using their energies, it is not possible to define a corresponding angular motion. This is a second advantage of DMD over POD in the post-processing of experimental data.

The conclusions made for the double-rotating state apply to reacting flows as well. Once again the flow can be approximated with a smaller number of POD modes. However, DMD of multiple nominally identical sets of snapshots aided differentiation between robust and non-robust dynamical modes and, hence, reproducible and non-reproducible flow characteristics. As in the co-rotating state, a "phase" of the dynamical modes was defined using their (time-dependent) coefficients. In bluff-body flows, it represents not an angular position, but the downstream displacement of the associated vortex. The phase dynamics were found to be highly regular compared to the (erratic) changes in the magnitude of the coefficients.

Using phase dynamics and Lissajous figures, strongly correlated modes that were associated with a single flow constituent were identified. Thus, it was possible to differentiate between symmetric and asymmetric vortex shedding and reconstruct these constituents of the complex reacting flow.

The ability to identify reproducible flow constituents and select dynamic modes associated with a flow constituent is helpful in constructing reduced-order models for combustion flows. Construction of these models is based on the dynamics, symmetries, and topological features of the reproducible flow constituents, which must be supplemented by the statistical features of noise and other non-reproducible aspects of the flow.

VI. ACKNOWLEDGMENTS

Appendix A: Dynamic and Proper Orthogonal Modes

This Appendix outlines a set of conditions under which a combination of DMD modes with the same spatial structure is a POD mode of the spatio-temporal dynamics. Consider first spatio-temporal dynamics containing only a single dynamic mode $\Phi(\mathbf{x})$ with an eigenvalue λ. Since flows on an attractor have no growth or decay, the growth rates of the DMD modes have zero real parts; let $\lambda = i\mu$, where $\mu \in \mathbb{R}$. Thus, the (real) spatio-temporal field is

$$u(\mathbf{x}, t) = e^{i\mu t}\Phi(\mathbf{x}) + e^{-i\mu t}\Phi^*(\mathbf{x}). \tag{A1}$$

Noting that the time average $\langle e^{i\mu t}\rangle_t \sim \delta_{\mu 0}$, the correlation matrix is

$$C_{\mathbf{x},\mathbf{x}'} = \langle u(\mathbf{x}, t)u(\mathbf{x}', t)\rangle_t = \Phi(\mathbf{x})\Phi^*(\mathbf{x}') + \Phi^*(\mathbf{x})\Phi(\mathbf{x}'), \tag{A2}$$

where $\mathbf{x}$ and $\mathbf{x}'$ are two spatial locations. Consequently,

$$\sum_{\mathbf{x}'} C_{\mathbf{x},\mathbf{x}'}\Phi(\mathbf{x}') = N\alpha\Phi(\mathbf{x}) + N\beta\Phi^*(\mathbf{x}), \tag{A3}$$

where $\alpha = \langle\Phi^*(\mathbf{x}')\Phi(\mathbf{x}')\rangle_{\mathbf{x}'} \in \mathbb{R}$, $\beta = \langle\Phi(\mathbf{x}')\Phi(\mathbf{x}')\rangle_{\mathbf{x}'} \in \mathbb{C}$, and N is the total number of grid points.

Consider a "phase-advanced" (or in the case of the cellular state, rotated) pattern $e^{i\theta}\Phi(\mathbf{x})$ whose real part is $\Phi_R(\mathbf{x}) \equiv e^{i\theta}\Phi(\mathbf{x}) + e^{-i\theta}\Phi^*(\mathbf{x})$. Using Eqn. (A3) and its complex conjugate

$$\sum_{\mathbf{x}'} C_{\mathbf{x},\mathbf{x}'}\Phi_R(\mathbf{x}') = N\left[\alpha e^{i\theta} + \beta^* e^{-i\theta}\right]\Phi(\mathbf{x}) + N\left[\alpha e^{-i\theta} + \beta e^{i\theta}\right]\Phi^*(\mathbf{x}). \tag{A4}$$

Choosing $\theta = (i/4)\ln(\beta/\beta^*)$, $\sum_{\mathbf{x}'} C_{\mathbf{x},\mathbf{x}'}\Phi_R(\mathbf{x}') \sim \Phi_R(\mathbf{x})$ and, hence, $\Phi_R(\mathbf{x})$ is an eigenfunction of $C_{\mathbf{x},\mathbf{x}'}$; *i.e.,* the phase-advanced dynamic mode is a POD mode.

Next, we extend the result to a field formed by a linear combination of a set of dynamic modes with the same spatial structure. As before, the effective real part of the corresponding eigenvalues is zero. The corresponding spatio-temporal pattern can be written as

$$u(\mathbf{x},t) = \left(\sum_k c_k e^{i\mu_k t + i\theta_k}\right)\Phi(\mathbf{x}) + \left(\sum_k c_k^* e^{-i\mu_k t - i\theta_k}\right)\Phi^*(\mathbf{x}), \tag{A5}$$

where c_k is the coefficient and θ_k the phase of the kth DMD mode, with $e^{i\mu_k t}$ being its eigenvalue. Since the μ's are distinct, the corresponding correlation matrix is

$$C_{\mathbf{x},\mathbf{x}'} = \left(\sum_k |c_k|^2\right)\left[\Phi(\mathbf{x})\Phi^*(\mathbf{x}') + \Phi^*(\mathbf{x})\Phi(\mathbf{x}')\right]. \tag{A6}$$

It follows that a phase-advanced dynamic mode is a POD mode for the spatio-temporal dynamics.

Finally, we outline how the result generalizes to a spatio-temporal field with two dynamic modes. The generalization to multiple modes is straightforward. Denote the two dynamic modes by $\Phi_1(\mathbf{x})$ and $\Phi_2(\mathbf{x})$. The spatio-temporal field can be expressed as

$$u(\mathbf{x},t) = c_1 e^{i\mu_1 t}\Phi_1(\mathbf{x}) + c_2 e^{i\mu_2 t}\Phi_2(\mathbf{x}) + c.c., \tag{A7}$$

where c_1 and c_2 are the coefficients of the dynamic modes and *c.c.* represents the complex conjugate. The correlation matrix for the state is

$$C_{\mathbf{x},\mathbf{x}'} = |c_1|^2\Phi_1(\mathbf{x})\Phi_1^*(\mathbf{x}') + |c_1|^2\Phi_1^*(\mathbf{x})\Phi_1(\mathbf{x}') + |c_2|^2\Phi_2(\mathbf{x})\Phi_2^*(\mathbf{x}') + |c_2|^2\Phi_2^*(\mathbf{x})\Phi_2(\mathbf{x}'). \tag{A8}$$

Defining $\alpha_1 = \langle\Phi_1(\mathbf{x}')\Phi_1^*(\mathbf{x}')\rangle_{\mathbf{x}'} \in \mathbb{R}$, $\beta_1 = \langle\Phi_1(\mathbf{x}')\Phi_1(\mathbf{x}')\rangle_{\mathbf{x}'} \in \mathbb{C}$, $\gamma_1 = \langle\Phi_1(\mathbf{x}')\Phi_2^*(\mathbf{x}')\rangle_{\mathbf{x}'} \in \mathbb{C}$, and $\gamma_2 = \langle\Phi_1(\mathbf{x}')\Phi_2(\mathbf{x}')\rangle_{\mathbf{x}'} \in \mathbb{C}$, it is apparent that

$$\sum_{\mathbf{x}'} C_{\mathbf{x},\mathbf{x}'}\Phi_1(\mathbf{x}') = N\alpha_1\Phi_1(\mathbf{x}) + N\beta_1\Phi_1^*(\mathbf{x}) + N\gamma_1\Phi_2(\mathbf{x}) + N\gamma_2\Phi_2^*(\mathbf{x}). \tag{A9}$$

If the domains of $\Phi_1(\mathbf{x})$ and $\Phi_2(\mathbf{x})$ do not overlap (as is the case for the first two dynamic modes for the double rotating state [see Figures (9) and (11))], then $\gamma_1 = 0 = \gamma_2$. Now, Eqn. (A9) reduces to Eqn. (A3). Consequently, a phase-advanced dynamic mode is a principal component, as was noted in Section III.

---

[1] J. B. Heywood, Internal Combustion Engine Fundamentals, McGraw-Hill Science/Engineering/Math, McGraw-Hill, Inc., New York, 1988.

[2] Y. S. Matros, Unsteady Processes in Catalytic Reactors, Elsivier Science Publishers, Amsterdam–New York, 1985.

[3] G. A. Viswanathan, M. Sheintuch, D. Luss, Transversal Hot Zones Formation in Catalytic Packed-Bed Reactors, Industrial & Engineering Chemistry Research 47 (20) (2008) 7509–7523.

[4] G. Viswanathan, D. Luss, Moving transversal hot zones in adiabatic, shallow packed-bed reactors, AICHE Journal 52 (2) (2006) 705–717.

[5] M. Gorman, M. elHamdi, K. Robbins, Chaotic Dynamics Near the Extinction Limit of a Premixed Flame on a Porous Plug Burner, Combustion Science and Technology 98 (1–3) (1994) 47–56.

[6] T. Lieuwen, Modeling premixed combustion-acoustic wave interactions: A review, Journal of Propulsion and Power 19 (5) (2003) 765–781.

[7] J. Hertzberg, I. Shepherd, L. Talbot, Vortex Shedding Behind Rod Stabilized Flames, Combustion and Flame 86 (1–2) (1991) 1–11.

[8] F. P. Incropera, D. P. deWitt, T. L. Bergman, A. S. Lavine, Fundamentals of Heat and Mass Transfer, John Wiley and Sons, Hoboken, N. J., 1990.

[9] E. Motheau, Y. Mery, F. Nicoud, T. Poinsot, Analysis and Modeling of Entropy Modes in a Realistic Aeronautical Gas Turbine, Journal of Engineering for Gas Turbines and Power–Transactions of the ASME 135 (9).

[10] S. Chandrasekhar, Hydrodynamic and Hydromagnetic Stability, Dover Publications, Inc., New York, 1961.

[11] P. G. Drazin, W. H. Reid, Hydrodynamic Stability, Cambridge University Press, Cambridge, 1981.

[12] F. Nicoud, K. Wieczorek, About the zero Mach number assumption in the calculation of

thermoacoustic instabilities, International Journal of Spray and Combustion Dynamics 1 (1) (2009) 67–111.

[13] S. Kostka, A. C. Lynch, B. C. Huelskamp, B. V. Kiel, J. R. Gord, S. Roy, Characterization of flame-shedding behavior behind a bluff-body using proper orthogonal decomposition, Combustion and Flame 159 (9) (2012) 2872–2882.

[14] P. Petersson, R. Wellander, J. Olofsson, H. Carlsson, C. Carlsson, B. B. Watz, N. Boestkjaer, M. Richter, M. Alden, L. Fuchs, X.-S. Bai, Simultaneous high-speed PIV- and OH-PLIF measurements and modal analysis for investigating flame–flow interactions in low swirl flames, 16th International Symposium on Applications of Laser Techniques to Fluid Mechanics, Lisbon, Portugal (9–12 July 2012).

[15] E. Ott, C. Grebogi, J. Yorke, Controlling Chaos, Physical Review Letters 64 (11) (1990) 1196–1199.

[16] T. Shinbrot, C. Grebogi, E. Ott, J. Yorke, Using Small Perturbations to Control Chaos, Nature 363 (6428) (1993) 411–417.

[17] A. Garfinkel, W. Ditto, M. Spano, J. Weiss, Control of Cardiac Chaos, Circulation 86 (4, S) (1992) 217217.

[18] A. Garfinkel, M. Spano, W. Ditto, J. Weiss, Controlling Cardiac Chaos, Science 257 (5074) (1992) 1230–1235.

[19] R. Roy, T. Murphy, T. Maier, Z. Gills, E. Hunt, Dynamic Control of a Chaotic Laser – Experimental Stabilization of a Globally Coupled System, Physical Review Letters 68 (9) (1992) 1259–1262.

[20] S. Schiff, K. Jerger, D. Duong, T. Chang, M. Spano, W. Ditto, Controlling Chaos in the Brain, Nature 370 (6491) (1994) 615–620.

[21] S. Schiff, K. Jerger, T. Chang, T. Sauer, P. Aitken, Stochastic Versus Deterministic Variability in Simple Neuronal Circuits. 2. Hippocampal Slice, Biophysical Journal 67 (2) (1994) 684–691.

[22] S. Narayanan, G. H. Gunaratne, F. Hussain, A dynamical systems approach to the control of chaotic dynamics in a spatiotemporal jet flow, Chaos 23 (3) (2013) 033133.

[23] P. Cvitanović, G. H. Gunaratne, I. Procaccia, Topological and metric properties of Hénon-type strange attractors, Physical Review A 38 (3) (1988) 1503–1520.

[24] D. Auerbach, P. Cvitanović, J.-P. Eckmann, G. Gunaratne, I. Procaccia, Exploring chaotic motion through periodic orbits, Physical Review Letters 58 (23) (1987) 2387–2389.

[25] S. Bagheri, P. Schlatter, P. J. Schmid, D. S. Henningson, Global stability of a jet in crossflow, Journal of Fluid Mechanics 624 (2009) 33–44.

[26] C. W. Rowley, I. Mezic, S. Bagheri, P. Schlatter, D. S. Henningson, Spectral analysis of nonlinear flows, Journal of Fluid Mechanics 641 (2009) 115–127.

[27] A. Palacios, G. Gunaratne, M. Gorman, K. Robbins, Cellular Pattern Formation in Circular Domains, Chaos 7 (3) (1997) 463–475.

[28] J.-C. Hua, G. H. Gunaratne, S. Kostka, N. Jiang, B. V. Kiel, J. R. Gord, S. Roy, Dynamical-systems analysis and unstable periodic orbits in reacting flows behind symmetric bluff bodies, Physical Review E 88 (3) (2013) 033011.

[29] L. Sirovich, Turbulence and the Dynamics of Coherent Structures .1. Coherent Structures, Quarterly of Applied Mathematics 45 (3) (1987) 561–571.

[30] L. Sirovich, Turbulence and the Dynamics of Coherent Structures .2. Symmetries and Transformations, Quarterly of Applied Mathematics 45 (3) (1987) 573–582.

[31] L. Sirovich, Turbulence and the Dynamics of Coherent Structures .3. Dynamics and Scaling, Quarterly of Applied Mathematics 45 (3) (1987) 583–590.

[32] J. L. Lumley, The Structure of Inhomogeneous Flow in "Atmospheric Turbulence and Radio Wave Propagation," Publishing House Nauka, Moscow (1967) pp. 166–176.

[33] P. J. Schmid, Dynamic mode decomposition of numerical and experimental data, Journal of Fluid Mechanics 656 (2010) 5–28.

[34] I. Mezic, Analysis of Fluid Flows via Spectral Properties of the Koopman Operator, in: Davis, SH and Moin, P (Ed.), Annual Review of Fluid Mechanics, Vol 45, Vol. 45 of Annual Review of Fluid Mechanics, 2013, pp. 357–378.

[35] M. Bergmann, C. H. Bruneau, A. Lollo, Enablers for robust POD models, Journal of Computational Physics 228 (2) (2009) 516–538.

[36] P. J. Schmid, Dynamic mode decomposition of experimental data, 8th International Symposium on Particle Image Veocimetry – PIV09, Melbourne, Victoria (2009).

[37] G. Gunaratne, M. el-Hamdi, M. Gorman, K. Robbins, Asymmetric Cells and Rotating Rings in Cellular Flames, Modern Physics Letters B 10 (28) (1996) 1379–1387.

[38] G. Dangelmayr, D. Armbruster, Classification Of Z(2)-Equivariant Imperfect Bifurcations With Corank-2, Proceedings of the London Mathematical Society 46 (May) (1983) 517–546.

[39] R. Goldstein, G. Gunaratne, L. Gil, P. Coullet, Hydrodynamic and Interfacial Patterns with

Broken Space–Time Symmetry, Physical Review A 43 (12) (1991) 6700–6721.

[40] T. Lieuwen, J. Cho, Coherent acoustic wave amplification/damping by wrinkled flames, Journal of Sound and Vibration 279 (3–5) (2005) 669–686.

[41] L.-Z. Huang, D.-M. Nie, Vortex Shedding Patterns in Flow Past Inline Oscillating Elliptical Cylinders, Thermal Science 16 (5) (2012) 1395–1399.

[42] E. Konstantinidis, S. Balabani, Symmetric vortex shedding in the near wake of a circular cylinder due to streamwise perturbations, Journal of Fluids and Structures 23 (7) (2007) 1047–1063.

[43] A. W. Caswell, N. Jiang, S. Roy, B. C. Huelskamp, J. R. Monfort, A. C. Lynch, V. Belovich, J. R. Gord, High-repetition-rate OH-PLIF and PIV measurements in bluff body stabilized flames, AIAA SciTech, American Institute of Aeronautics and Astronautics, AIAA 2014-0733 (2014).

[44] J. H. Tu, C. W. Rowley, D. M. Luchtenburg, S. L. Brunton, J. N. Kutz, On Dynamic Mode Decomposition: Theory and Applications. http://arxiv.org/pdf/1312.0041v1.pdf.